

Theory of the Magnon Parametron

Mehrdad Elyasi,¹ Eiji Saitoh,^{1,2,3,4,5} and Gerrit E. W. Bauer^{1,2,3,6}

¹*Institute for Materials Research, Tohoku University, Sendai 980-8577, Japan*

²*WPI Advanced Institute for Materials Research, Tohoku University, Sendai 980-8577, Japan*

³*Center for Spintronics Research Network, Tohoku University, Sendai 980-8577, Japan*

⁴*Department of Applied Physics, University of Tokyo, Hongo, Tokyo 113-8656, Japan*

⁵*Advanced Science Research Center, Japan Atomic Energy Agency, Tokai 319-1195, Japan*

⁶*Zernike Institute for Advanced Materials, University of Groningen, 9747 AG Groningen, Netherlands*

(Dated: January 11, 2022)

The ‘magnon parametron’ is a ferromagnetic particle that is parametrically excited by microwaves in a cavity. Above a certain threshold of the microwave power, a bistable steady state emerges that forms an effective Ising spin. We calculate the dynamics of the magnon parametron as a function of microwave power, applied magnetic field and temperature for the interacting magnon system, taking into account thermal and quantum fluctuations. We predict three dynamical phases, viz. a stable Ising spin, telegraph noise of thermally activated switching, and an intermediate regime that at lower temperatures is quantum correlated with significant distillable magnon entanglement. These three regimes of operation are attractive for alternative computing schemes.

An Ising spin is a magnetic moment with a large uniaxial anisotropy that reduces the quantum degree of freedom of the Heisenberg spin on the Bloch sphere to just two, i.e. up and down. More generally, the term is used for any bistable system with a phase space of two distinct and stable configurations. For example, the magnetization of a fixed ferromagnetic needle that can point only into the two directions that minimizes the free energy is a (pseudo) Ising spin. An Ising spin with noise-activated transitions can operate as a probabilistic bit (p-bit), which in its steady state is a statistical mixture of the two levels. Ising spins are not useful as qubits because the large energy barrier prevents spin rotations on the Bloch sphere. Nevertheless, interactions with other degrees of freedom can induce quantum coherence of the Ising up and down spins and entanglement with other excitations. An ensemble of spins in these three regimes form a platform for unconventional computing algorithms. Switchable, but thermally stable, Ising spins are elements of “Ising machines” that can solve hard optimization problems [1–5], while network of p-bits can factorize large integers [6]. A relatively large (~ 2000) and highly connected network of pseudo Ising spins with phase measurement and feedback was implemented by a train of optical parametric oscillators [2–4]. However, optical implementations have a large footprint and are not scalable. Quantum coherent networks are even more difficult to realize, but they can perform additional tasks such as quantum annealing, adiabatic evolution, or gated quantum operations [7–12].

Parametric pumping is a standard method to excite large oscillations in a harmonic oscillator by a phase matched drive at twice the resonance frequency ω_0 . When a harmonic oscillator with Hamiltonian $\hbar\omega_0 a^\dagger a$, where a^\dagger (a) creates (annihilates) a boson, has non-linear interaction with photons, it can be driven into an instability by the parametric term $P e^{2i\omega_0 t} a^\dagger a^\dagger + \text{H.c.}$, when

the classical amplitude P exceeds a certain threshold. In the steady state, the mean field $\langle a \rangle$ spontaneously acquires either one of the energetically equivalent phases of $\phi_p/2 + 0$ or $\phi_p/2 + \pi$, where $\phi_p = \arg P e^{2i\omega_0 t}$ and $2 \bmod \arg[\langle a \rangle, 2\pi] = \bmod[\phi_p, 2\pi]$, which can be mapped on the two states of a pseudo Ising spin. Such oscillators can be realized by optical [2–4], electromechanical [13], or magnetic [14] systems. Makiuchi et al. [14] demonstrated a “magnon parametron” on a disk of the magnetic insulator yttrium iron garnet (YIG) that also showed the stochastic behavior expected for a p-bit.

A Hilbert space of a quantum system is ‘discrete’ when its dimension is countable, e.g., two for a spin-1/2 system. It is called ‘continuous’ when uncountably infinite, e.g. when spanned by position and momentum variables of a harmonic oscillator. The lowest number states of the Kittel magnons, i.e. the quanta of the uniform precession of the magnetic order [15–17] enable ‘discrete variable’ quantum information processing [18, 19]. However, since their anharmonicity is small, an auxiliary superconducting qubit is required to manipulate the quantum states of the lowest magnon levels. On the other hand, strongly driven magnons alone offer ‘continuous variable’ quantum information such as entanglement, photon squeezing, and antibunching [20–22]. Magnons are also set apart from e.g. phonons [23] by their highly tunable, anisotropic and non-monotonic dispersions. Parametric excitation of magnets generates large magnon numbers that live long enough to form Bose-Einstein condensates [24–27]. We are especially interested in the efficient and distillable entanglement of magnons [21] in the parametrically excited regime.

In this Letter, we address the theory of the ‘magnon parametron’ [14], i.e. a thin film magnetic disc that is parametrically excited in a microwave cavity. We show that it can operate as an Ising spin that is tuned between deterministic, stochastic, and quantum regimes,

which should be considered seriously as a platform for alternative computing technologies. The Suhl instability [21, 28], i.e. the decay of the uniform (Kittel) magnon into a pair of magnons with opposite momenta $\pm k \neq 0$, can be reached by driving magnon parametrically by cavity-mode microwaves with a small amplitude when quality factors are high. At a classical fixed point of the magnetization dynamics and at cryogenic temperatures we predict a distillable quantum entanglement [21]. The limit-cycle dynamics at slightly higher photon amplitudes enables the observed stochastic switching between the Ising spin states [14] only when the ‘wing’ magnons are involved.

Model - Figure 1(a) sketches a thin ferromagnetic disk of thickness d and radius r , uniformly magnetized along the in-plane magnetic field $\vec{H}_{ext} \parallel \hat{z}$. The microwave magnetic field $\vec{h}_{mw} \parallel \hat{z}$ of a cavity or a coplanar waveguide mode with frequency ω_p is polarized along the magnetization. Figure 1(b) shows the magnon frequency dispersions $\omega_{\vec{k}}$ of a typical YIG disk of $d = 50$ nm, corresponding to $\theta_{\vec{k}} = 0$ ($\vec{k} \parallel \hat{z}$) and $\theta_{\vec{k}} = \pi/2$ ($\vec{k} \perp \hat{z}$) for in-plane wave vectors and constant magnetization along \hat{x} , i.e. the lowest magnon subband [29–31]. ω_0 is the frequency of the Kittel mode. A node along \hat{x} blue-shifts the entire dispersion $\sim 4\gamma D/d^2 \sim 0.2$ GHz relative to the bulk value of Fig. 1(b), where $\gamma = 26$ GHz/T is the gyromagnetic ratio and $D = 2 \times 10^{-17}$ Tm² is the exchange stiffness [32]. We restrict our study to the lowest subband since for the chosen dimensions $\omega_{\vec{k}_{dip}} + 4\gamma D/d^2 > \omega_0$, where $\omega_{\vec{k}_{dip}}$ is the frequency minimum caused by the magnetodipolar interaction. The two valleys in the magnon dispersion are essential for the Suhl instability and exist when $r \gtrsim 0.5 \mu\text{m}$.

Figure 1(b) sketches the Kittel mode and a degenerate pair of magnons with wave vector $\pm \mathcal{K}$ as well as the four-magnon scattering process relevant to a Suhl instability. $\vec{h}_{mw}(t)$ with frequency $\omega_p = 2\omega_0$ parametrically interacts with the Kittel mode and the degenerate magnon pairs. Our Hamiltonian contains the leading terms of the Holstein-Primakoff expansion of the Heisenberg model,

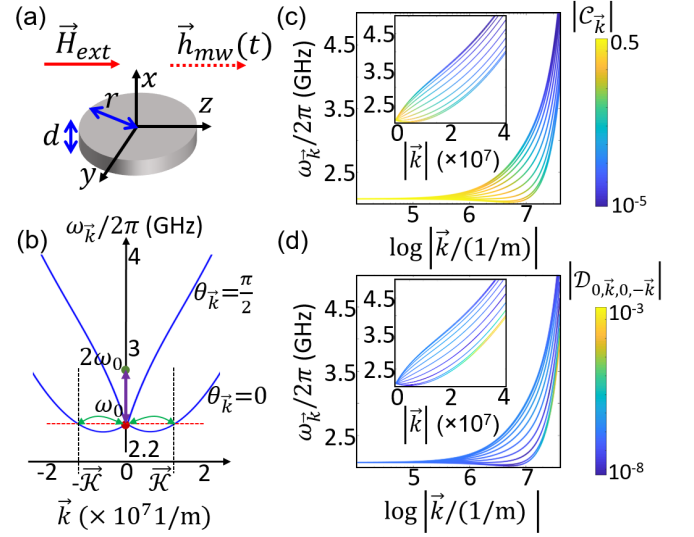


FIG. 1. Model. (a) A magnetic disk of thickness d and radius r under static and microwave magnetic fields. (b) The dispersion envelope of magnons with constant magnetization along x for $d = 50$ nm and $r = 100 \mu\text{m}$. The green arrows indicate 4-magnon scattering processes involving the Kittel mode. The purple line indicates parametric pumping of the Kittel mode. (c) The parametric excitation coefficient amplitude $C_{\vec{k}}$ of the magnon pairs overlaid on the dispersion for several values of $\theta_{\vec{k}}$ from 0 to $\pi/2$, only for the modes nodeless along the thickness. (d) Similar to (c) but for the 4-magnon scattering coefficient $\mathcal{D}_{0,\vec{k},0,-\vec{k}}$. The insets of (c) and (d) plot the data of the main panels on a linear momentum scale..

including all 4-magnon interactions [21, 33, 34]

$$\begin{aligned}
 H &= H_{m,L} + H_{m,NL} + H_{mp} + H_p, \\
 H_{m,L} &= \sum_{\vec{k}} \omega_{\vec{k}} c_{\vec{k}}^\dagger c_{\vec{k}}, \\
 H_{m,NL} &= \sum_{\vec{k}} \left\{ \mathcal{D}_{\vec{k},\vec{k},\vec{k},\vec{k}} c_{\vec{k}}^\dagger c_{\vec{k}}^\dagger c_{\vec{k}} c_{\vec{k}} + \right. \\
 &\quad \sum_{\vec{k}''} \left[\left(1 - \delta_{\vec{k},\vec{k}''} \right) \mathcal{D}_{\vec{k},\vec{k},\vec{k}'',-\vec{k}''} c_{\vec{k}}^\dagger c_{\vec{k}}^\dagger c_{\vec{k}''} c_{-\vec{k}''} + \right. \\
 &\quad \left. \left(1 - \delta_{|\vec{k}|,|\vec{k}''|} \right) \frac{1}{2} \mathcal{D}_{\vec{k},\vec{k}'',-\vec{k},-\vec{k}''} c_{\vec{k}}^\dagger c_{-\vec{k}}^\dagger c_{\vec{k}''} c_{-\vec{k}''} \right] \Big\}, \\
 H_{mp} &= \sum_{\vec{k}} \frac{1}{2} \left(1 + \delta_{\vec{k},0} \right) \left(\mathcal{G}_{\vec{k}} b c_{-\vec{k}}^\dagger c_{\vec{k}}^\dagger + H.c. \right), \\
 H_p &= \omega_p b^\dagger b + E \left(b^\dagger + b \right), \tag{1}
 \end{aligned}$$

where $\mathcal{G}_{\vec{k}} = \gamma C_{\vec{k}} \sqrt{\hbar \mu_0 \omega_p / 2 V_p}$, b is the photon annihilation operator, V_p is the cavity mode volume, $m_z = 1 - \sum_{\vec{k}} \left[c_{\vec{k}}^\dagger c_{\vec{k}} + \left(c_{\vec{k}}^\dagger c_{-\vec{k}}^\dagger + H.c. \right) \right] / S$ is the \hat{z} component of the magnetization unit vector, the total spin $S = M_s V_m / 2\pi \gamma \hbar$, V_m is the volume of the sample, M_s is the saturation magnetization. The coefficients \mathcal{C} and \mathcal{D} are complicated but well known [33, 34].

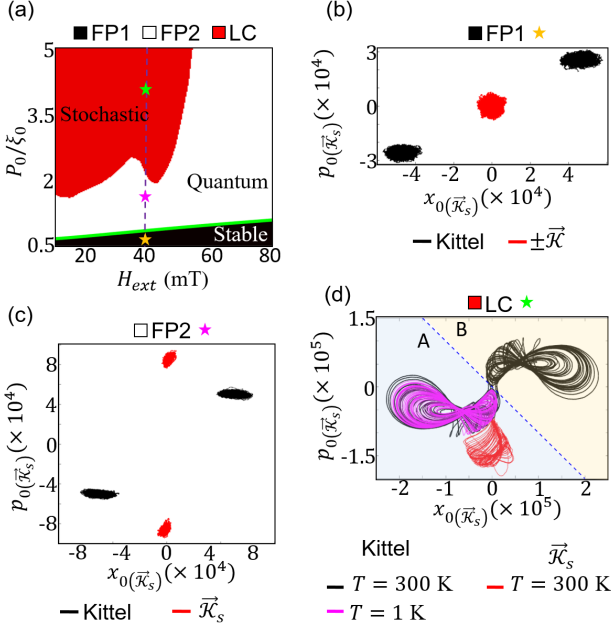


FIG. 2. Calculated steady-state dynamics of a magnet in a microwave cavity. (a) The dependence of steady-state class on the Kittel mode amplitude P_0 driven by the microwaves and the dc magnetic field H_{ext} , labeled as ‘Stable’, ‘Quantum’, and ‘Stochastic’. (b)-(d) Examples for the three distinct classes, corresponding to the stars of the same color in in (a), $P_0/\xi_0 = 0.7, 1.7, 3.8$, respectively, while $H_{ext} = 40$ mT. (b) FP1: Fixed point, the Kittel mode parametrically driven beyond threshold, while the \vec{k}_s pair at vacuum. FP2: Fixed point, the Kittel mode and \vec{k}_s standing wave parametrically and Suhl instability driven, respectively. In (b) and (c), $T = 3 \times 10^5$ K for clarity. (d) LC: Limit cycle to chaos. A case with large transition rate from one attractor region of the Kittel mode to the other, at $T = 300$ K, and no transition for $T = 1$ K also shown. The two attractor regions A and B indicated. In (b) and (c), green trajectories are for \vec{k} standing wave.

Here we pump the precession cone angle of spin waves by the microwave magnetic field along the magnetization. The photon drive E with $\omega_p \sim 2\omega_0$ leads to a coherent photon field $\langle b \rangle = \beta$ such that $\mathcal{G}_{\vec{k}}\beta c_{-\vec{k}}^\dagger c_{\vec{k}}^\dagger + \text{H.c.}$ can parametrically excite the Kittel mode and magnon pairs with $\omega_{\vec{k}} \sim \omega_p/2$. When increasing E , the mode with the largest $\mathcal{G}_{\vec{k}} \propto C_{\vec{k}}$ becomes unstable at a critical value $\mathcal{G}_{\vec{k}}\beta = \xi_{\vec{k}}/2$, where $\xi_{\vec{k}} \approx \alpha_G \omega_{\vec{k}}$ is the magnon dissipation rate in terms of α_G , the Gilbert damping constant. $|C_{\vec{k}}|$ in Figure 1(c) is maximal for small wave vectors, which implies that the Kittel mode becomes unstable first. The “drift” matrix $\mathcal{O} = [i\omega_0 - \xi_0/2, i\mathcal{G}_0\beta; -i\mathcal{G}_0\beta, -i\omega_0 - \xi_0/2]$ of the linear equation of motion $[\dot{c}_0, \dot{c}_0^\dagger]^T = \mathcal{O}[c_0, c_0^\dagger]^T$ then acquires an eigenvalue with positive real part. The so-called self-Kerr coefficient $\mathcal{D}_{0,0,0,0}$ governs steady state Kittel magnon amplitude just above the threshold. Here we use rather large damping parameter $\xi_0 = 5$ MHz cor-

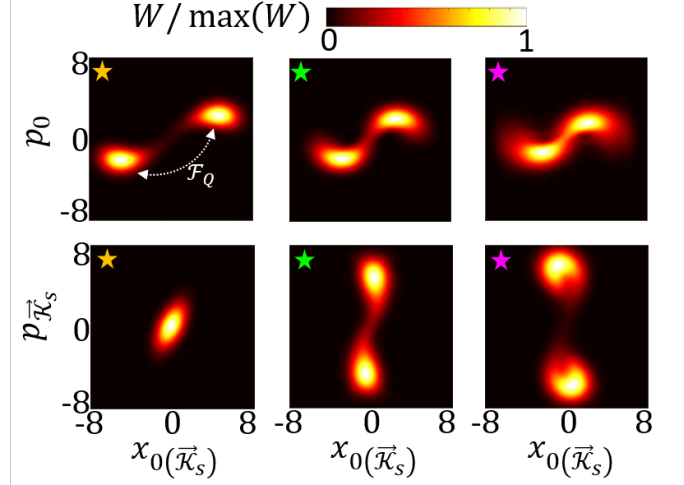


FIG. 3. Quantum steady states. The top (bottom) panels are the Wigner function of the Kittel mode (\vec{k} standing wave) normalized by the maximum value. The left, middle, and right panels correspond to the star of the same color as in Fig. 2(a), as well as Figs. 2(b)-(d), i.e., in the FP1 (Ising), ‘Quantum’ (FP2), and ‘Stochastic’ (LC) regions, respectively. The scaling of four-magnon scattering coefficients $\mathcal{Q} = 5 \times 10^8, 2 \times 10^9, 4 \times 10^9$, from left to right panels, respectively.

responding to $\alpha_G \sim 2 \times 10^{-3}$ for computational convenience.

The parametrically driven Kittel mode excites other magnons via the four-magnon scattering term $c_0^\dagger c_0^\dagger c_{-\vec{k}} c_{-\vec{k}} + \text{H.c.}$, where Fig. 1(d) plots the corresponding coefficients $|\mathcal{D}_{0,\vec{k},0,-\vec{k}}|$. This is another threshold process introduced first by Suhl [28]. Ignoring the terms $c_0^\dagger c_0 c_{\pm\vec{k}}^\dagger c_{\pm\vec{k}}$ for the moment, the instability is reached when the amplitude of the Kittel mode mean field $|\alpha_0| = \langle c_0 \rangle = \left(\sqrt{\xi_k^2/4 + \Delta_k^2} / |\mathcal{D}_{0,\vec{k},0,-\vec{k}}| \right)^{1/2}$. This happens first for the degenerate modes with largest $|\mathcal{D}_{0,\vec{k},0,-\vec{k}}|$, i.e. for $\theta_{\vec{k}} = 0$ and large $|\vec{k}|$ and thereby limits the Hilbert space to three modes, the parametrically pumped Kittel mode and a pair of magnons with large wave vector $\pm\vec{k}$. In the rotating frame of $\omega_p/2$, the Hamiltonian (1) reduces to $H' = H'_{m,L} + H'_{m,NL} + P_0 (c_0^\dagger c_0^\dagger + \text{H.c.})$, where $H_{m,L} = \sum_{\vec{k} \in \{0, \pm\vec{k}\}} \Delta \omega_{\vec{k}} c_{\vec{k}}^\dagger c_{\vec{k}}$, $\Delta \omega_{\vec{k}} = \omega_{\vec{k}} - \omega_p/2$, $H'_{m,NL} = H_{m,NL}|_{\vec{k} \in \{0, \pm\vec{k}\}}$. The critical parametric excitation amplitude $P_0 = \xi_0/2$ corresponds to a photon amplitude $E \approx P_0 \xi_p / 2 \mathcal{G}_0$ and power $\mathcal{P} = E^2 \hbar \omega_p / \xi_p = P_0^2 \xi_p \hbar \omega_p / 4 \mathcal{G}_0^2$. Assuming $\xi_p = 10$ kHz (photon quality factor $\sim 10^5$), and $\mathcal{G}_{\vec{k}}/C_{\vec{k}} = 10$ which corresponds to a photon mode volume $V_p \sim 10^{-2} \text{ mm}^3$, for $P_0 = \xi_0/2$, $\mathcal{P} \approx 2 \mu\text{W}$ and for $P_0 = 5\xi_0$ (maximum value used in our calculations), $\mathcal{P} \approx 0.2 \text{ mW}$.

The (Lindblad) equation of motion of the density ma-

trix ρ with elements $\rho_{i,j} = |i\rangle\langle j|$, where $|i(j)\rangle$ is a many-body number (Fock) state of the magnon system, reads

$$\dot{\rho} = -i[H', \rho] + L_d, \quad (2)$$

where

$$L_d = \sum_{\vec{k} \in \{0, \pm\mathcal{K}\}} \xi_{\vec{k}} \left[n_{th}(\omega_{\vec{k}}) \left(c_{\vec{k}} \rho c_{\vec{k}}^\dagger + c_{\vec{k}}^\dagger \rho c_{\vec{k}} - \rho c_{\vec{k}}^\dagger c_{\vec{k}} - c_{\vec{k}}^\dagger c_{\vec{k}} \rho \right) + \frac{1}{2} \left(2c_{\vec{k}} \rho c_{\vec{k}}^\dagger - c_{\vec{k}}^\dagger c_{\vec{k}} \rho - \rho c_{\vec{k}}^\dagger c_{\vec{k}} \right) \right], \quad (3)$$

is the dissipation operator of the magnons in contact with a thermal bath. Here $n_{th}(\omega_{\vec{k}}) = (e^{\hbar\omega_{\vec{k}}/k_B T} - 1)^{-1}$, k_B is the Boltzmann constant, and T is the bath temperature. We disregard nonlinear radiative damping terms since $|\gamma C_{\vec{k}} \sqrt{\hbar\mu_0\omega_p/2V_p}|^2/\xi_p \xi_0 \ll 1$ [35]. Without drive, ρ describes a magnon gas at thermal equilibrium with the bath.

Next, we show our results for the driven steady state, quantify stochasticity, and discuss quantum entanglement in our magnetic dot.

Steady state classes - We classify the steady state dynamics in terms of a “phase diagram” of our three-mode system by the solutions of the Langevin equation of motion. Disregarding the third and fourth order derivatives of the Wigner distribution functions as described in the supplementary material (SM), Sec. I [36–38] for small nonlinearities, simplifies the equation of motion to $\dot{v} = -i[H, v] + \Gamma$, where $v = [x_0, p_0, x_{\mathcal{K}}, p_{\mathcal{K}}, x_{-\mathcal{K}}, p_{-\mathcal{K}}]$, $x_{0(\pm\vec{\mathcal{K}})} = (c_{0(\pm\vec{\mathcal{K}})} + c_{0(\pm\vec{\mathcal{K}}}^\dagger)/2$, $p_{0(\pm\vec{\mathcal{K}})} = -i(c_{0(\pm\vec{\mathcal{K}})} - c_{0(\pm\vec{\mathcal{K}}}^\dagger)/2$, and Γ represents fluctuating fields with Gaussian quantum statistics. We solve this 6-dimensional Langevin differential equation in real time starting from appropriate initial conditions until the steady state is reached.

The microwaves parametrically excite the Kittel mode with detuning $\Delta\omega_0 = 0$, and an amplitude P_0 . The other control parameter is the applied static magnetic field H_{ext} . The smallest positive solution for $x = |\alpha_0|^2$ governs $\theta_{\vec{\mathcal{K}}}$ and $|\vec{\mathcal{K}}|$ of the magnon pair that reaches the Suhl instability first

$$\left(\mathcal{D}_{0,\vec{\mathcal{K}},0,-\vec{\mathcal{K}}}^2 - \mathcal{D}_{0,0,\vec{\mathcal{K}},\vec{\mathcal{K}}}^2 \right) x^2 - 2\Delta_{\vec{\mathcal{K}}} \mathcal{D}_{0,0,\vec{\mathcal{K}},\vec{\mathcal{K}}} x - \xi_{\vec{\mathcal{K}}}^2/4 - \Delta_{\vec{\mathcal{K}}}^2 = 0. \quad (4)$$

Below the Suhl but above the parametric instability threshold $|\alpha_0|^2 = \sqrt{P_0^2 - \xi_0^2/4}/2|\mathcal{D}_{0,0,0,0}|$.

With notation $c_{\pm\mathcal{K}} = |c_{\pm\mathcal{K}}|e^{i\phi_{\pm\mathcal{K}}}$, the four magnon scatterings fix the sum of the phases $\phi_+ = \phi_{\vec{\mathcal{K}}} + \phi_{-\vec{\mathcal{K}}}$, but the difference $\phi_- = \phi_{\vec{\mathcal{K}}} - \phi_{-\vec{\mathcal{K}}}$ is not uniquely determined [40]. The magnetic disc has a large but finite radius, that strictly speaking splits the continuum of state by $\Delta\nu \sim 2n\gamma D/r^2 \sim 10^4 \text{ Hz}$, where $n = \lfloor 2r\mathcal{K} \rfloor \sim 4000$. Since $\Delta\nu \ll \xi_0$, the spectrum is still quasi-continuous,

but the Kittel mode decays not into two propagating, but a single standing wave mode. This can be formalized by combining the $\pm\vec{\mathcal{K}}$ pair of propagating waves as $c_{\pm\vec{\mathcal{K}}} = c_{\vec{\mathcal{K}}_s} e^{\mp iq/2}$ [39, 40], where the phase $q = \phi_-$ is a free phase that governs the position of the standing wave nodes and $\vec{\mathcal{K}}_s$ is a standing wave index. This reduction of a three-partite into a two-partite problem simplifies the quantum regime calculations.

Figure 2(a) shows the steady state classes as a function of H_{ext} and P_0 , obtained numerically for $T = 0 \text{ K}$. The green line in Fig. 2(a) is an analytic solution of Eq. (4) using the four-magnon scattering parameters of the unstable mode for each H_{ext} . The phase-space dynamics of each class are illustrated by Figs. 2(b)-(d) for a fixed magnetic field. Figures 2(b) and (c) show trajectories in the time interval $t = 50 - 80 \mu\text{s}$, starting from 100 random initial values of $\phi_{0(\vec{\mathcal{K}}_s)}$ in $c_{0(\vec{\mathcal{K}}_s)} = e^{i\phi_{0(\vec{\mathcal{K}}_s)}}$ at $t = 0$ and a high temperature $T = 3 \times 10^5 \text{ K}$ to emphasize the dynamic stability. The trajectories are depicted in $(x_{0(\vec{\mathcal{K}}_s)}, p_{0(\vec{\mathcal{K}}_s)})$ phase space. We observe two distinct classes that are characterized by Kittel mode fixed-points FP1 and FP2. For a given H_{ext} and small $P_0 > \xi_0/2$ (FP1) the Kittel mode has two equivalent stable fixed points (Ising spin up and down), while $\vec{\mathcal{K}}_s$ standing wave mode only fluctuates around the origin [see Fig. 2(b)]. When P_0 satisfies Eq. (4), the Suhl instability drives the $\pm\mathcal{K}$ pair, leading to the FP2 steady state in which the Kittel fixed points persist, and $\vec{\mathcal{K}}_s$ settles at a fixed point away from the origin with a phase spontaneously chosen out of two mirror symmetric values [see Fig. 2(c)]. We note that even though FP2 is labeled “quantum”, at the chosen high temperatures all quantum correlations are of course washed out (see below). A third distinct class without a stable fixed point is the limit cycle (LC) illustrated in Figure 2(d) for realistic temperatures. For certain H_{ext} and not too large P_0 , the Kittel mode follows large amplitude trajectories in mirror symmetric regions of the phase space (see also SM Sec. IV [38]). With increasing P_0 the paths cross the boundaries between attractor regions A and B. The thermal activation becomes clear from Figure 2(d) that compares switching at high $T = 300 \text{ K}$ (black curve), and low $T = 1 \text{ K}$ (purple curve), where we show single representative trajectories in the interval $t = 20 - 320 \mu\text{s}$. We elaborate this stochasticity below. In SM Sec. IV [38], we discuss the dependence of the limit cycle trajectories on P_0 (see Fig. S4 [38]), and analytically explain the origin of FP2 to LC transition, and its dependence on H_{ext} (see Fig. S5 [38]).

The Lindblad master equation can be solved in principle numerically exact in number (Fock) space. With our computational facilities the Hilbert space has to be limited to ~ 1000 , which is much too small to treat the essential Hilbert space of a large magnet. We can reduce the Hilbert space to a manageable size by introducing a scaling factor of the four-magnon scattering coefficients $\mathcal{D} \rightarrow$

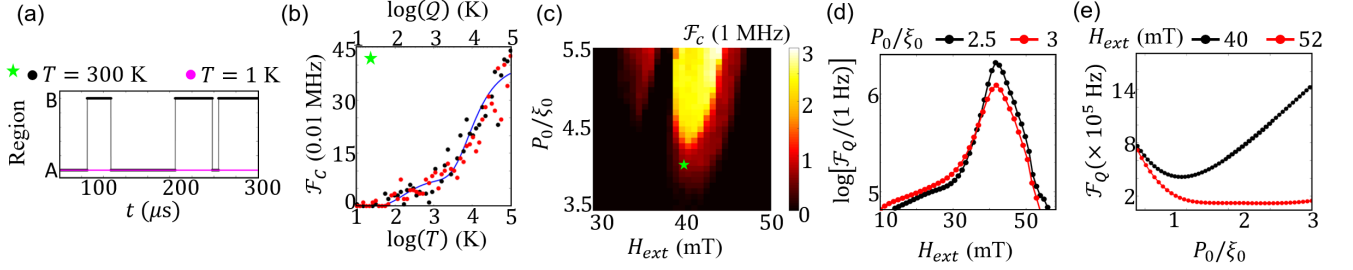


FIG. 4. Stochasticity. (a)-(c) From semi-classical, (d)-(f) from quantum calculations. (a) The region of the Kittel mode state shown in Fig. 2(d) for $T = 1$ K and $T = 300$ K. (b) The dependence of transition frequency \mathcal{F}_C on T (black dots) and \mathcal{Q} (red dots), for $H_{\text{ext}} = 40$ mT, $P_0/\xi_0 = 3.85$, as in (a) and Fig. 2(d). (c) \mathcal{F}_C as a function of H_{ext} and P_0/ξ_0 , at $T = 3 \times 10^5$ K. The green star is the same (P_0, H_{ext}) point as in the phase diagram plotted in Figs. 2(a) and (d). (d) The dependence of tunneling frequency \mathcal{F}_Q on H_{ext} for two values of $P_0/\xi_0 = 2.5, 3$. (e) The dependence of \mathcal{F}_Q on P_0/ξ_0 for $H_{\text{ext}} = 40, 52$ mT, respectively. The scaling coefficient $\mathcal{Q} = 5 \times 10^9$ in (d)-(e), and $T = 0$ K.

\mathcal{QD} with $\mathcal{Q} \gg 1$. The increased interaction preserves the topology in phase space, but reduces the magnon amplitudes and thereby the relevant size of the Fock space. As explained above, selecting the standing wave \vec{K}_s , reduces the 3-mode to a 2-mode problem. We calculate up to 20 smallest amplitude eigenvalues $\mathcal{E} \geq 0$ of the r.h.s. of Eq. (2), in which the $\mathcal{E} = 0$ corresponds to the ground state density matrix ρ_{ss} . We visualize the steady states by the Wigner distribution function $W(x_0(\vec{K}_s), p_0(\vec{K}_s)) = \int \langle x_0(\vec{K}_s) - y/2 | \rho_{ss,0}(\vec{K}_s) | x_0(\vec{K}_s) + y/2 \rangle e^{ip_0(\vec{K}_s)y} dy$ of the Kittel (\vec{K}_s) mode, where $|x_0(\vec{K}_s) \pm y/2\rangle$ is the position eigenstate of the Kittel (\vec{K}_s) mode, and $\rho_{ss,0}(\vec{K}_s)$ is the density matrix after tracing out the \vec{K}_s (Kittel) mode. The top (bottom) panels of Fig. 3 show $W(x_0(\vec{K}_s), p_0(\vec{K}_s))$ for $H_{\text{ext}} = 40$ mT in each of the ‘Stable’, ‘Quantum’, and ‘Stochastic’ phases, as indicated by stars of the same color in Fig. 2(a). The left and middle panels can be compared with the classical phase space of FP1 and FP2 in Figs. 2(b) and (c), respectively. The right panel of Fig. 3 should be compared with the limit cycle region in the classical phase space, e.g., in Fig. 2(c). In the panels of Fig. 3, we used different scale factors \mathcal{Q} such that the distance between the extrema of W is roughly the same.

The steady state classes FP1, FP2, and LC [see Fig. 2(a)] are potential resources for information technologies. For a fixed input power of P_0 the stable Ising spin can be used as a non-volatile digital memory, while a network can operate as an Ising machine. We can assess the potential of the device as p-bit or for quantum information by quantitative measures of the stochasticity and entanglement derived from our semi-classical (quantum) calculations indicated in the following by a subscript or superscript ‘C’ (‘Q’). In ‘C’, we solve the quantum Langevin equation of motion for Gaussian distribution functions. In the quantum calculations, on the other hand, we solve the master equation (2) in the number (Fock) space, and the solutions are numerically exact, but due to computa-

tional limitations we can solve only down-scaled systems, as explained above.

Stochasticity - The lower bound for the transition time τ between the two stable fixed points below the Suhl instability threshold (derived in SM Sec. IIB [38]) is

$$\ln \tau \gtrsim \ln \left[\pi (1 + 2n_{\text{th}}) \sqrt{(1 + 2\mathcal{R})/2\mathcal{R}^2/2\xi_0} \right] + \frac{[(2\mathcal{R} + 1) \ln(2\mathcal{R} + 1) - 2\mathcal{R}] |K_0| (1 + 2n_{\text{th}})}{2}, \quad (5)$$

where $\mathcal{R} = \sqrt{\mu^2 - 1}/2 + 1 - |K_0| (1 + 2n_{\text{th}}) - 1$, $\mu = 2P_0/\xi_0$, $K_0 = 2\mathcal{D}_{0,0,0,0}/\xi_0$. Above the parametric instability threshold but below the Suhl instability ($\mu = 1.1$) for typical values of $|\mathcal{D}_{0,0,0,0}| = 1.5 \times 10^{-4}$ Hz (see Fig. S5(a) [38]), $\omega_0/2\pi = 2.5$ GHz [see Fig. 1(b)], and $T = 300$ K, this number becomes astronomically large, $\tau \gg \exp(1.4 \times 10^4)$ s. However, by driving the system into a limit cycle of the Kittel plus $\pm \mathcal{K}$ modes at sufficiently large μ we find a strongly enhanced switching rate at room temperature [see Fig. 2(d)]. The experimental observation of stochastic switching [14] is therefore strong evidence for a parametrically driven Suhl instability in the magnon parametron.

The telegraph noise of the Kittel mode at $T = 300$ K in Figure 4(a) is caused by thermally activated random hoppings as in Fig. 2(d). The calculated number of switches N_t within $t_e = 100 \mu\text{s}$, averaged for several random initial conditions leads to the transition frequencies $\mathcal{F}_C = N_t/t_e$ plotted in Figure 4(b) as a function of T (black dots). The form $l_1 e^{-\lambda_1/T} + l_2 e^{-\lambda_2/T}$, with attempt frequencies $l_1 = 32$ Hz, $l_2 = 8.1$ Hz, and energy well depths $\lambda_1 = 7.98 \times 10^3 \times k_B/2\pi\hbar$ GHz, $\lambda_2 = 1.5 \times 10^2 \times k_B/2\pi\hbar$ GHz fits the calculations well (blue curve). We also compute the transition frequency dependence at $T = 1$ K on \mathcal{Q} , a scaling number of the four-magnon scattering coefficient \mathcal{QD} that is inversely proportional to the volume of the magnet V_m . The red dots in Figure 4(b) show that we can enhance the switching rate by either increasing the temperature or decreasing the volume. Figure 4(d) shows the

dependence of \mathcal{F}_C on H_{ext} and P_0 at $T = 10^5$ K. Makiuchi *et al.* [14] observed switching frequencies $\sim 0.01 - 0.1$ Hz at room temperature, depending on the power beyond a second threshold. As explained above, this is not possible without the Suhl instability. Even though the sample in that experiment is larger than directly accessible with our model, we can still draw conclusions from the identical scaling for T and \mathcal{Q} observed in Fig. 4(b). By repeating the calculations for a scaling factor $\mathcal{Q} = 1/30$, we effectively address a magnet that is 30 times larger compared to $\mathcal{Q} = 1$. The result of $\mathcal{F}_C \sim 0.01$ Hz at $T = 300$ K agrees with the lower end of the experimental observations. The predicted strong and non-monotonic dependence of \mathcal{F}_C on H_{ext} in Fig. 4(c) also agrees with experimental findings. The substantial enhancement of the stochasticity is due to the limit cycle dynamics with large oscillation amplitudes which come in close vicinity of the saddle node in the origin. Since a limit cycle broadens the distribution function when compared to a fixed point, the thermally activated switching through the saddle node becomes more efficient. At a fixed H_{ext} , increasing P_0 leads to increasing LC oscillation amplitude and LC doublings (see Fig. S4 [38]), and therefore an increase in \mathcal{F} is expected. Due to the dependence of \mathcal{D} coefficients on H_{ext} (see Fig. S5(a) [38]), at a fixed P_0 , the amplitude of the LC oscillations depends on H_{ext} , and has a maximum at $H_{\text{ext}} \sim 40$ mT [see SM Sec. IV and Fig. S5(d) [38]], where the maximum of both \mathcal{F}_C and \mathcal{F}_Q is observed [see Figs. 4(c) and (d)]. In future work we will address a quantitative theory for large magnetic dots that take into account perpendicular standing spin waves and three-magnon scatterings.

Next, we quantify the stochasticity from quantum calculations, i.e. \mathcal{F}_Q . The first two eigenvalues with smallest but nonzero $|\text{Re}\mathcal{E}|$ while $\text{Im}\mathcal{E} = 0$, determine the tunneling frequencies (see SM Sec. IIA [38]). One of these eigenvalues corresponds to the tunneling frequency of the Kittel mode, \mathcal{F}_Q [35] [see top left panel of Fig. 3(a)], as explained in SM Sec. IIA [38]. The other corresponds to the tunneling frequency of the \vec{K}_s mode. Below parametric instability, and below Suhl instability threshold, such eigenvalue does not exist for either of the modes, and the \vec{K}_s mode, respectively.

Figure 4(d) shows \mathcal{F}_Q as a function of H_{ext} for two values of $P_0/\xi_0 = 2.5, 3$ that crosses both the LC and FP2 regions [see Fig. 2(a)]. \mathcal{F}_Q is peaked at $H_{\text{ext}} \sim 40$ mT similar to that of \mathcal{F}_C in Fig. 4(c), and decreases sharply for H_{ext} in the FP2 region. Figure 4(e) shows that \mathcal{F}_Q decreases monotonically with increasing P_0 for $H_{\text{ext}} = 52$ mT where the classical steady state does not enter the LC region. However, for $H_{\text{ext}} = 40$ mT, where the steady state changes from FP1 to FP2, and then becomes LC, by increasing P_0 , \mathcal{F}_Q first decreases and then increases substantially. Based on the fit in Eq. 4(b), for $\mathcal{Q} = 10^9$, $\mathcal{F}_C \sim 1$ MHz, which is in the same range as expected from \mathcal{F}_Q in Figs. 4(d) and (e). The calculated stochastic

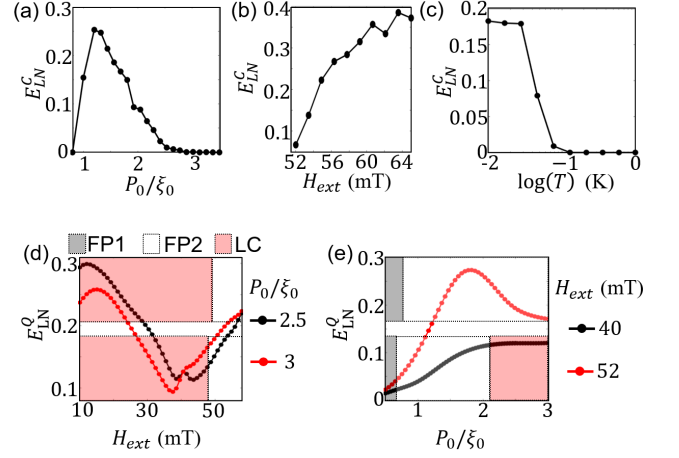


FIG. 5. Entanglement. (a)-(c) From semi-classical, (d)-(e) from quantum calculations. (a) Gaussian logarithmic negativity E_{LN}^G dependence on P_0/ξ_0 for $H_{\text{ext}} = 52$ mT and $T = 0$ K. (b) The dependence of E_{LN}^G on H_{ext} for $P_0/\xi_0 = 2$ and $T = 0$ K. (c) The dependence of E_{LN}^G on T for $H_{\text{ext}} = 52$ mT and $P_0/\xi_0 = 2$. (d) The dependence of logarithmic negativity E_{LN}^Q , on H_{ext} for two values of $P_0/\xi_0 = 2.5, 3$. (e) The dependence of E_{LN}^Q on P_0/ξ_0 for $H_{\text{ext}} = 40, 52$ mT. The scaling coefficient $\mathcal{Q} = 5 \times 10^9$ and $T = 0$ K in (d)-(e). The steady state class from Fig. 2(a) corresponding to each point is shown by color coded rectangles, where top (bottom) rectangles are for red (black) dots.

ticsities of the Kittel mode are the same for propagating or standing exchange waves in the large dot limit.

Quantum entanglement - The driven quantum state is a many-body wave function in which the fluctuations of two types of magnons may become quantum entangled. At the steady-state fixed points of both Kittel and \vec{K}_s modes beyond the Suhl instability threshold, the cross Kerr interaction $c_0^\dagger c_0 c_{\vec{K}_s}^\dagger c_{\vec{K}_s} + \text{H.c.}$ can be approximated by $\alpha_0^* \alpha_{\vec{K}_s}^* \delta c_0 \delta c_{\vec{K}_s} + \text{H.c.}$, where $\alpha_0(\vec{K}_s)$ is mean field value of the Kittel (\vec{K}_s) mode, and δc indicates fluctuations. Under the conditions discussed below, this “two-mode squeezing” term leads to quantum correlations. In the SM Sec. III [38], we discuss the corrections by the “beam-splitter” interaction.

The quantum correlations that characterize entanglement become apparent in the noise statistics. The “quantumness” of the system [41] can be measured by the mean-square fluctuations

$$\sigma = \left\langle \left(\delta x_0 - \delta x_{\vec{K}_s} \right)^2 + \left(\delta p_0 + \delta p_{\vec{K}_s} \right)^2 \right\rangle = \xi_0 \frac{n_{\text{th}} + \frac{1}{2}}{2\mathbf{g} + \xi_0} \quad (6)$$

where $\mathbf{g} = \left| \mathcal{D}_{0,0,\pm\vec{K},\pm\vec{K}} \alpha_0^* \alpha_{\vec{K}_s}^* \right|$ (see SM Sec. III [38]). In the regime $0 \leq \sigma < 1/2$, the two modes are necessarily quantum-correlated or “entangled”. When the modes do not interact $\mathbf{g} = 0$, $\sigma \rightarrow n_{\text{th}} + 1/2$. In general, uncorre-

lated and classical states correspond to $\sigma \geq 1/2$. When \mathbf{g} becomes large, the fluctuations and σ vanish, which reflects commutation of the operators for the relative positions and momenta $[\delta x_0 - \delta x_{\vec{k}_s}, \delta p_0 + \delta p_{\vec{k}_s}] = 0$ in that limit. $\sigma \propto (n_{\text{th}} + 1/2)$ illustrates how increasing temperature destroys quantum correlations by pushing the system into the classical regime $\sigma > 1/2$ irrespective of the interactions. This allows us to estimate the experimental conditions to observe quantum entanglement in realistic systems, see below and SM Sec. III [38].

For an accurate assessment of the bipartite quantum entanglement between the Kittel and \vec{k}_s magnons fluctuations all mean-field terms of equal order must be included, which can be done only numerically. Moreover, σ is not a good measure of the entanglement resource. More suitable is the “logarithmic negativity” function E_{LN} that increases monotonically with the degree of entanglement [42]. This parameter is measure of the negativity of the partial transposition of the density matrix (with respect to the Kittel mode) $\rho^{PT} = \rho_0^T \otimes \rho_{\vec{k}_s}$ that vanishes when the bipartite state is separable. $E_{LN} = \log_2(1 + 2|\mathbf{n}|)$, where \mathbf{n} is the sum of the negative eigenvalues of ρ^{PT} . E_{LN} is an upper bound of the “distillable” entanglement E_D , which is again a measure for the number of completely entangled pairs of quasiparticles (singlets) that can be extracted from the many-body wave function by local operations and classical communications [41, 43, 44], which are essential for e.g. quantum teleportation and quantum key distribution [7, 41, 45, 46]. The density matrix of a Gaussian state, i.e. a localized state in phase space or fixed point, is completely determined by the first and second moments of position and momentum variables, i.e. the covariance matrix, via which E_{LN} can be readily calculated [42, 47] (see SM Sec. III [38]). $E_{LN} = 0$ for a separable bipartite state and it diverges for $\sigma = 0$. In realistic systems usually $E_{LN} < 1$ [48, 49]. Here, we calculate the steady state covariance matrix \mathcal{V}_{ss} by ensemble averaging over 100 independent 50 μs runs starting from random initial conditions over the last 1 μs . Figures 5(a)-(c) summarize results of the Gaussian logarithmic negativity E_{LN}^C calculated via \mathcal{V}_{ss} for some of the FP2 cases identified earlier. Here the superscript C indicates the Gaussian assumption. In Figure 5(a), we observe that E_{LN}^C as a function of P_0 , for $H_{\text{ext}} = 52 \text{ mT}$ and zero temperature, is zero below the Suhl instability threshold (at $P_0/\xi_0 = 0.92$) and peaks at relatively small P_0 . Figure 5(b) shows that for a fixed $P_0/\xi_0 = 2$, E_{LN}^C increases strongly with H_{ext} (see Fig. S5) up to about ~ 0.5 . According to Figure 5(c) E_{LN}^C decreases with increasing T , but remains nearly constant up to $T \approx 100 \text{ mK}$. In SM Sec. III and Fig. S3 [38], we support these observations by an analytical analysis.

The entanglement of Gaussian states may be computed by the semi-classical approach. When nonlinearities drive the fluctuations beyond Gaussian statistics, we

have to solve the quantum master equation for the steady state density matrix ρ_{ss} . The elements of ρ_{ss} correspond to $|i, j\rangle\langle i', j'|$, where i (i') and j (j') refer to the i 'th (i' 'th) and j 'th (j' 'th) Fock (number) state of the Kittel (\vec{k}_s) mode, and we require the sum of the negative eigenvalues of the partially transposed density matrix with elements $|i', j\rangle\langle i, j'|$. Figure 5(d) shows that E_{LN}^Q (superscript Q for quantum) is non-monotonic in H_{ext} . It turns out to be minimal when the quantum stochasticity \mathcal{F}_Q in Figure 4(d) is maximal. The phase space occupied by an LC is much larger than that of the quantum fluctuations, hence distilling the entanglement is not feasible. Therefore, only the entanglement in the FP2 region is useful. Figure 5(d) shows that E_{LN}^Q increases with H_{ext} in the FP2 region, similar to Fig. 5(b). Figure 5(e) shows that with decreasing P_0 towards FP1 region, E_{LN}^Q approaches zero. It can also be seen that it has a peak in P_0 for $H_{\text{ext}} = 52 \text{ mT}$ similar to Fig. 5(a).

In order to measure and distill the entanglement, both the Kittel mode and the large wave vector magnon pair should resonantly couple to microwaves. This can be achieved by a coplanar waveguide that is modulated with the wave length of the wing magnons that locks the otherwise undetermined phase difference ϕ between the $\pm\vec{k}$ pair, i.e. the nodes of the standing wave magnon amplitude [21].

Conclusion - We study the bistable nature of the Ising spin system emulated by ferromagnetic disk parametrically excited in a microwave cavity as a function of temperature, magnetic field, and excitation power. The Suhl decay of the Kittel mode into a degenerate pair of magnons with large wave vector substantially enhances the random switching between the two energy minima of the Kittel mode parametron phase space, providing a probabilistic bit for stochastic information processing. On the other hand, the Suhl instability is also responsible for a finite distillable entanglement, which is a fundamental resource for quantum information. We show that the three regimes of operation are accessible by varying the parametric excitation power as well as the external magnetic field. The quantum correlations in macroscopic magnets should be observable at low but experimentally accessible temperatures of $\sim 100 \text{ mK}$. We conclude that magnetic particles are attractive building blocks for coherent Ising machines, as well as stochastic and quantum information applications.

Acknowledgments - We acknowledge support by JSPS KAKENHI (Nos. 19H00645 and 21K13847), and JST CREST (No. JPMJCR20C1).

-
- [1] M. Yamaoka, C. Yoshimura, M. Hayashi, T. Okuyama, H. Aoki, and H. Mizuno, “A 20k-Spin Ising Chip to Solve Combinatorial Optimization Problems With CMOS An-

- nealing”, IEEE J. Solid-State Circuits **51**, 303 (2015).
- [2] T. Inagaki et al., “Large-scale Ising spin network based on degenerate optical parametric oscillators”, Nat. Phys. **10**, 415 (2016).
 - [3] T. Inagaki et al., “A coherent Ising machine for 2000-node optimization problems”, Science **354**, 603 (2016).
 - [4] P. L. McMahon, A. Marandi, Y. Haribara, R. Hamerly, C. Langrock, S. Tamate, T. Inagaki, H. Takesue, S. Utsunomiya, K. Aihara, R. L. Byer, M. M. Fejer, H. Mabuchi, Y. Yamamoto “A fully programmable 100-spin coherent Ising machine with all-to-all connections”, Science **354**, 614 (2016).
 - [5] D. Pierangeli et al., “Large-Scale Photonic Ising Machine by Spatial Light Modulation”, Phys. Rev. Lett. **122**, 213902 (2019).
 - [6] W. A. Borders, A. Z. Pervaiz, S. Fukami, K. Y. Cam-sari, H. Ohno, and S. Datta, “Integer factorization using stochastic magnetic tunnel junctions”, Nature **573**, 390 (2019).
 - [7] M. A. Nielsen and I. L. Chuang, *Quantum computation and quantum information*, Cambridge Univ. Press, Cambridge (2009).
 - [8] D. P. DiVincenzo, *Quantum Computation*, Science **270**, 255 (1995).
 - [9] T. Albash and D. A. Lidar, “Adiabatic quantum computation”, Rev. Mod. Phys. **90**, 015002 (2018).
 - [10] E. Farhi et al., “A Quantum Adiabatic Evolution Algorithm Applied to Random Instances of an NP-Complete Problem”, Science **292**, 472 (2001).
 - [11] S. Boixo et al., “Evidence for quantum annealing with more than one hundred qubits”, Nat. Phys. **10**, 218 (2014).
 - [12] M. W. Johnson, M. H. S. Amin, S. Gildert, T. Lanting, F. Hamze, N. Dickson, R. Harris, A. J. Berkley, J. Johansson, P. Bunyk, E. M. Chapple, C. Enderud, J. P. Hilton, K. Karimi, E. Ladizinsky, N. Ladizinsky, T. Oh, I. Perminov, C. Rich, M. C. Thom, E. Tolkacheva, C. J. S. Truncik, S. Uchaikin, J. Wang, B. Wilson, and G. Rose, “Quantum annealing with manufactured spins”, Nature **473**, 194 (2011).
 - [13] I. Mahboob, H. Okamoto, and H. Yamaguchi, “An electromechanical Ising Hamiltonian”, Sci. Adv. **2**, e1600236 (2016).
 - [14] T. Makiuchi, T. Hioki, Y. Shimazu, Y. Oikawa, N. Yokoi, S. Daimon, and E. Saitoh, “Parametron on magnetic dot: Stable and stochastic operation”, Appl. Phys. Lett. **118**, 022402 (2021).
 - [15] X. Zhang, C.-L. Zou, L. Jiang, and H. X. Tang, *Strongly Coupled Magnons and Cavity Microwave Photons*, Phys. Rev. Lett. **113**, 156401 (2014).
 - [16] H. Huebl, C. W. Zollitsch, J. Lotze, F. Hocke, M. Greifenstein, A. Marx, R. Gross, and S. T. B. Goennenwein, *High Cooperativity in Coupled Microwave Resonator Ferrimagnetic Insulator Hybrids*, Phys. Rev. Lett. **111**, 127003 (2013).
 - [17] Y. Tabuchi, S. Ishino, T. Ishikawa, R. Yamazaki, K. Usami, and Y. Nakamura, *Hybridizing Ferromagnetic Magnons and Microwave Photons in the Quantum Limit*, Phys. Rev. Lett. **113**, 083603 (2014).
 - [18] Y. Tabuchi, S. Ishino, A. Noguchi, T. Ishikawa, R. Yamazaki, K. Usami, and Y. Nakamura, *Coherent Coupling Between a Ferromagnetic Magnon and a Superconducting Qubit*, Science **349**, 405 (2015).
 - [19] D. Lachance-Quirion, S. P. Wolski, Y. Tabuchi, S. Kono, K. Usami, and Y. Nakamura, Science **367**, 425 (2020).
 - [20] J. Li, S.-Y. Zhu, and G. S. Agarwal, Phys. Rev. Lett. **121**, 203601 (2018).
 - [21] M. Elyasi, Y. M. Blanter, G. E. W. Bauer, Phys. Rev. B **101**, 054402 (2020).
 - [22] H. Y. Yuan and Rembert A. Duine, Phys. Rev. B **102**, 100402 (2020).
 - [23] M. Aspelmeyer, T. J. Kippenberg, and F. Marquardt, *Cavity Optomechanics*, Rev. Mod. Phys. **86**, 1391 (2014).
 - [24] V. E. Demidov, O. Dzyapko, S. O. Demokritov, G. A. Melkov, and A. N. Slavin, *Thermalization of a Parametrically Driven Magnon Gas Leading to Bose-Einstein Condensation*, Phys. Rev. Lett. **99**, 037205 (2007).
 - [25] V. E. Demidov, O. Dzyapko, S. O. Demokritov, G. A. Melkov, and A. N. Slavin, *Observation of Spontaneous Coherence in Bose-Einstein Condensate of Magnons*, Phys. Rev. Lett. **100**, 047205 (2008).
 - [26] A. A. Serga, V. S. Tiberkevich, C. W. Sandweg, V. I. Vasyuchka, D. A. Bozhko, A. V. Chumak, T. Neumann, B. Obry, G. A. Melkov, A. N. Slavin, and B. Hillebrands, *Bose-Einstein Condensation in an Ultra-Hot Gas of Pumped Magnons*, Nat. Commun. **5**, 3452 (2013).
 - [27] D. A. Bozhko, A. A. Serga, P. Clausen, V. I. Vasyuchka, F. Heussner, G. A. Melkov, A. Pomyalov, V. S. Lvov, and B. Hillebrands, *Supercurrent in a Room-Temperature Bose-Einstein Magnon Condensate*, Nat. Phys. **12**, 1057 (2016).
 - [28] H. Suhl, *The Theory of Ferromagnetic Resonance at High Signal Powers*, Phys. Chem. Solids **1**, 209 (1957).
 - [29] S. M. Rezende, *Theory of Coherence in Bose-Einstein Condensation Phenomena in a Microwave-Driven Interacting Magnon Gas*, Phys. Rev. B **79**, 174411 (2009).
 - [30] B. A. Kalinikos and A. N. Slavin, *Theory of Dipole-Exchange Spin Wave Spectrum for Ferromagnetic Films with Mixed Exchange Boundary Conditions*, J. Phys. C: Solid State Phys. **19**, 7013 (1986).
 - [31] M. J. Hurben and C. E. Patton, *Theory of Magnetostatic Waves for in-Plane Magnetized Isotropic Films*, J. Magn. Mater. **139**, 263 (1995).
 - [32] D. D. Stancil and A. Prabhakar, *Spin Waves*, Springer (2009).
 - [33] P. Krivosik and C. E. Patton, “Hamiltonian formulation of nonlinear spin-wave dynamics: Theory and applications”, Phys. Rev. B **82**, 184428 (2010).
 - [34] S. M. Rezende “Fundamentals of magnonics”, Springer (2020).
 - [35] P. Kinsler and P. D. Drummond, “Quantum dynamics of the parametric oscillator”, Phys. Rev. A **43**, 6194 (1991).
 - [36] H. J. Carmichael, *Statistical Methods in Quantum Optics*, Springer (1999).
 - [37] D. F. Walls and G. J. Milburn, *Quantum Optics*, Springer (2008).
 - [38] See supporting material [URL will be inserted by publisher] for derivation of equations of motion from the master equation, calculation of tunneling frequency from quantum master equation solution, analytical discussion on tunneling frequency of a fixed point parametron, analytical quantification of the Gaussian entanglement, demonstration of limit cycle evolution and doublings, analytical explanation of the steady state phase diagram including the fixed point to limit cycle bifurcation, and correlation of limit cycle oscillation amplitude with Kittel mode parametron tunneling frequency.
 - [39] P. H. Bryant, C. D. Jeffries, and K. Nakamura, *Spin-*

- Wave Dynamics in a Ferrimagnetic Sphere*, Phys. Rev. A **38**, 4223 (1988).
- [40] V. E. Zakharov, V. S. L'vov, and S. S. Starobinets, *Spin-wave turbulence beyond the parametric excitation threshold*, Sov. Phys. Usp. **17**, 896 (1974).
 - [41] S. L. Braunstein and P. van Loock, *Quantum Information with Continuous Variables*, Rev. Mod. Phys. **77**, 513 (2005).
 - [42] G. Vidal and R. F. Werner, *Computable Measure of Entanglement*, Phys. Rev. A **65**, 032314 (2002).
 - [43] C. H. Bennett, H. J. Bernstein, S. Popescu, and B. Schumacher, *Concentrating Partial Entanglement by Local Operations*, Phys. Rev. A **53**, 2046 (1996).
 - [44] M. Horodecki, P. Horodecki, and R. Horodecki, *Inseparable Two Spin- $\frac{1}{2}$ Density Matrices Can Be Distilled to a Singlet Form*, Phys. Lett. A **223**, 1 (1996).
 - [45] S. L. Braunstein, and H. J. Kimble, *Teleportation of Continuous Quantum Variables*, Phys. Rev. Lett. **80**, 869 (1998).
 - [46] A. Furusawa, J. L. Sørensen, S. L. Braunstein, C. A. Fuchs, H. J. Kimble, and E. S. Polzik, *Unconditional Quantum Teleportation*, Science **282**, 706 (1998).
 - [47] G. Adesso and F. Illuminati, *Gaussian Measures of Entanglement versus Negativities: Ordering of Two-Mode Gaussian States*, Phys. Rev. A **72**, 032334 (2005).
 - [48] T. A. Palomaki, J. D. Teufel, R. W. Simmonds, and K. W. Lehnert, *Entangling Mechanical Motion with Microwave Fields*, Science **342**, 710 (2013).
 - [49] E. P. Menzel, R. D. Candia, F. Deppe, P. Eder, L. Zhong, M. Ihmig, M. Haeberlein, A. Baust, E. Hoffmann, D. Ballester, K. Inomata, T. Yamamoto, Y. Nakamura, E. Solano, A. Marx, and R. Gross, *Path Entanglement of Continuous-Variable Quantum Microwaves*, Phys. Rev. Lett. **109** 250502 (2012).

Theory of the Magnon Parametron: Supporting Material

Mehrdad Elyasi,¹ Eiji Saitoh,^{1,2,3,4,5} and Gerrit E. W. Bauer^{1,2,3,6}

¹*Institute for Materials Research, Tohoku University, Sendai 980-8577, Japan*

²*WPI Advanced Institute for Materials Research, Tohoku University, Sendai 980-8577, Japan*

³*Center for Spintronics Research Network, Tohoku University, Sendai 980-8577, Japan*

⁴*Department of Applied Physics, University of Tokyo, Hongo, Tokyo 113-8656, Japan*

⁵*Advanced Science Research Center, Japan Atomic Energy Agency, Tokai 319-1195, Japan*

⁶*Zernike Institute for Advanced Materials, University of Groningen, 9747 AG Groningen, Netherlands*

(Dated: January 11, 2022)

The following material explains several technical details that supplement the main text. In Sec. I, we derive the Langevin equation of motion from the Lindblad master equation. In Sec. II, we address the hopping frequency between the Ising spin states by the exact solutions of the quantum master equation [see Sec. II A], and by estimating its value for the Ising parametron in the classical limit [see Sec. II B]. In Sec. III, we present analytic approximations for the quantum entanglement between the Kittel and finite- k magnons that support the numerical results in the main text. In Sec. IV, we discuss the limit cycles in parameter space, explain its correlation with the hopping frequency of the Kittel mode, and with a simple analytical approach to the steady-state phase diagram spanned by the parametric excitation power and the applied magnetic field.

I. EQUATIONS OF MOTION

The starting point is the (Lindblad) equation of motion (EOM) of the density matrix ρ

$$\dot{\rho} = -i[H', \rho] + L_d, \quad (1)$$

where H' is the Hamiltonian for the interacting magnons in which the Kittel mode is driven by P_0

$$\begin{aligned} H' &= H'_{m,L} + H'_{m,NL} + \left(P_0 c_0^\dagger c_0^\dagger + H.c. \right), \\ H'_{m,L} &= \sum_{\vec{k} \in \{0, \pm\mathcal{K}\}} \Delta\omega_{\vec{k}} c_{\vec{k}}^\dagger c_{\vec{k}} \\ H'_{m,NL} &= \sum_{\vec{k} \in \{0, \pm\mathcal{K}\}} \left[\mathcal{D}_{\vec{k}, \vec{k}, \vec{k}} c_{\vec{k}}^\dagger c_{\vec{k}}^\dagger c_{\vec{k}} + \right. \\ &\quad \left. \sum_{\vec{k}' \in \{0, \pm\mathcal{K}\}} (1 - \delta_{\vec{k}, \vec{k}'}) \frac{1}{2} \mathcal{D}_{\vec{k}, \vec{k}, \vec{k}'} c_{\vec{k}}^\dagger c_{\vec{k}}^\dagger c_{\vec{k}'} + \right. \\ &\quad \left. \left[\mathcal{D}_{0, -\mathcal{K}, 0, \mathcal{K}} c_0^\dagger c_0^\dagger c_{-\mathcal{K}} c_{\mathcal{K}} + H.c. \right] \right], \end{aligned} \quad (2)$$

and

$$\begin{aligned} L_d &= \sum_{\vec{k} \in \{0, \pm\mathcal{K}\}} \xi_{\vec{k}} \left[n_{\text{th}}(\omega_{\vec{k}}) \left(c_{\vec{k}} \rho c_{\vec{k}}^\dagger + c_{\vec{k}}^\dagger \rho c_{\vec{k}} - \rho c_{\vec{k}}^\dagger c_{\vec{k}} - \right. \right. \\ &\quad \left. \left. c_{\vec{k}}^\dagger c_{\vec{k}} \rho \right) + \frac{1}{2} \left(2c_{\vec{k}} \rho c_{\vec{k}}^\dagger - c_{\vec{k}}^\dagger c_{\vec{k}} \rho - \rho c_{\vec{k}}^\dagger c_{\vec{k}} \right) \right], \end{aligned} \quad (3)$$

is their dissipation into a thermal bath. Here $n_{\text{th}}(\omega_{\vec{k}}) = (e^{\hbar\omega_{\vec{k}}/k_B T} - 1)^{-1}$, k_B is the Boltzmann constant, T is the bath temperature, and $\xi_{\vec{k}}$ are the dissipation rates.

We cover different regimes of the master equation (1) including the quantum-classical crossover in the form of an equation of motion for the Wigner quasi-probability distribution function

$$\begin{aligned} W(\alpha_0, \alpha_0^*, \alpha_{\vec{k}}, \alpha_{\vec{k}}^*, \alpha_{-\vec{k}}, \alpha_{-\vec{k}}^*) &= \frac{1}{\pi^2} \int d^2 z_{-\vec{k}} \int d^2 z_{\vec{k}} \\ &\int d^2 z_0 \text{tr} \left(\rho e^{iz_0^* c_0^\dagger} e^{iz_0 c_0} e^{iz_{\vec{k}}^* c_{\vec{k}}^\dagger} e^{iz_{\vec{k}} c_{\vec{k}}} e^{iz_{-\vec{k}}^* c_{-\vec{k}}^\dagger} e^{iz_{-\vec{k}} c_{-\vec{k}}} \right) \\ &e^{-iz_0^* \alpha_0^*} e^{-iz_0 \alpha_0} e^{-iz_{\vec{k}}^* \alpha_{\vec{k}}^*} e^{-iz_{\vec{k}} \alpha_{\vec{k}}} e^{-iz_{-\vec{k}}^* \alpha_{-\vec{k}}^*} e^{-iz_{-\vec{k}} \alpha_{-\vec{k}}}, \end{aligned} \quad (4)$$

where $z_{\vec{k}}$ and $\alpha_{\vec{k}}$ are complex variables, and $|\alpha_{\vec{k}}\rangle$ is the coherent state of mode \vec{k} . Following textbook procedures [1, 2]

$$\frac{\partial W}{\partial t} = \mathcal{W}_{HO} + \mathcal{W}_D + \mathcal{W}_{PE} + \mathcal{W}_{SK} + \mathcal{W}_{CK} + \mathcal{W}_S, \quad (5)$$

where the contributions on the r.h.s. represent, respectively, the non-interacting magnons

$$\mathcal{W}_{HO} = \sum_{k \in \{0, \pm\mathcal{K}\}} \left[k \Delta\omega_k \frac{\partial}{\partial \alpha_k} \alpha_k + H.c. \right] W, \quad (6)$$

the dissipation

$$\begin{aligned} \mathcal{W}_D &= \sum_{k \in \{0, \pm\mathcal{K}\}} \left[\frac{\xi_k}{2} \frac{\partial}{\partial \alpha_k} \alpha_k + \frac{\xi_k}{2} \frac{\partial}{\partial \alpha_k^*} \alpha_k^* + \right. \\ &\quad \left. \xi_k \left(n_{\text{th},k} + \frac{1}{2} \right) \frac{\partial^2}{\partial \alpha_k \partial \alpha_k^*} \right] W, \end{aligned} \quad (7)$$

the parametric excitation of the Kittel mode

$$\mathcal{W}_{PE} = \left[-iP_0 \frac{\partial}{\partial \alpha_0} \alpha_0^* + H.c. \right] W, \quad (8)$$

the self-Kerr interaction

$$\begin{aligned} \mathcal{W}_{SK} &= \sum_{k \in \{0, \pm\mathcal{K}\}} \left[i2\mathcal{D}_{k,k,k,k} \frac{\partial}{\partial \alpha_k} |\alpha_k|^2 \alpha_k + \right. \\ &\quad \left. \frac{1}{2} \frac{\partial^3}{\partial \alpha \partial \alpha_k^*{}^2} \alpha_k^* + H.c. \right] W, \end{aligned} \quad (9)$$

the cross-Kerr interactions

$$\mathcal{W}_{CK} = \sum_{k \in \{0, \pm \vec{\mathcal{K}}\}} \sum_{k' \in \{0, \pm \vec{\mathcal{K}}\}} k \mathcal{D}_{k, k', k'} (1 - \delta_{k, k'}) \left\{ \left[\frac{\partial}{\partial \alpha_k} |\alpha_{k'}|^2 \alpha_k + \frac{1}{4} \frac{\partial^3}{\partial \alpha_k \partial \alpha_k^* \partial \alpha_{k'}^*} \alpha_{k'}^* \right] + H.c. \right\} W, \quad (10)$$

and the 4-magnon interactions that drive the Suhl instability

$$\mathcal{W}_S = i \mathcal{D}_{0, \mathcal{K}, 0, -\mathcal{K}} \left[2 \frac{\partial}{\partial \alpha_0} \alpha_0^* \alpha_{\mathcal{K}} \alpha_{-\mathcal{K}} - \frac{\partial}{\partial \alpha_{-\mathcal{K}}^*} \alpha_0^2 \alpha_{\mathcal{K}} + \frac{\partial}{\partial \alpha_{\mathcal{K}}^*} \alpha_0^2 \alpha_{-\mathcal{K}} - \frac{1}{4} \frac{\partial^3}{\partial \alpha_0^2 \partial \alpha_{-\mathcal{K}}^*} \alpha_{\mathcal{K}} - \frac{1}{4} \frac{\partial^3}{\partial \alpha_0^2 \partial \alpha_{\mathcal{K}}^*} \alpha_{-\mathcal{K}} + \frac{1}{2} \frac{\partial^3}{\partial \alpha_0 \partial \alpha_{\mathcal{K}}^* \partial \alpha_{-\mathcal{K}}^*} \alpha_0^* + H.c. \right] W. \quad (11)$$

$\partial W / \partial \alpha_k$ is of the order of W when the latter is a peaked function such as a Gaussian. In our system the third order derivatives in Eqs. (9)-(11) are negligibly small since $|\mathcal{D} \alpha_k| \ll \xi_k (n_{\text{th}, k} + \frac{1}{2})$. Introducing $x_k = (\alpha_k + \alpha_k^*)/2$ and $p_k = -i(\alpha_k - \alpha_k^*)/2$, the Wigner EOM of Eq. (5) reduces to the Fokker-Planck equation (summing over repeated indices)

$$\dot{W}(\mathcal{X}) = -\frac{\partial}{\partial \mathcal{X}_i} \mathcal{A}_i(\mathcal{X}) + \frac{1}{2} \frac{\partial^2}{\partial \mathcal{X}_i \partial \mathcal{X}_j} D_{i,j}, \quad (12)$$

in the variables $\mathcal{X} = [x_0, p_0, x_{\mathcal{K}}, p_{\mathcal{K}}, x_{-\mathcal{K}}, p_{-\mathcal{K}}]$. $\mathcal{A}_i(\mathcal{X})$ in the first term (drift) follows by straightforward algebra from the first derivatives in Eqs. (5)-(10), while the second order derivatives in Eq. (7) lead to the second (diffusion) term with $D_{i,j} = \delta_{i,j} \xi_i (n_{\text{th}, k} + \frac{1}{2})$. The first and second moments obtained from the FPE can also be obtained as the solution of a set of associated (Ito) stochastic differential equations [1] in which diffusion is obtained by Wiener increments $dW_t = \Xi_i(t) dt$, i.e. the differentials of Markovian Wiener processes governed by the FPE with zero drift and unit diffusion, so

$$d\mathcal{X}_i = \mathcal{A}_i dt + \sqrt{\xi_i \left(n_{\text{th}, k} + \frac{1}{2} \right)} \Xi_i(t) dt, \quad (13)$$

where $\langle \Xi_i(t) \Xi_j(t') \rangle = \delta_{i,j} \delta(t, t')$.

II. HOPPING FREQUENCY

As explained in the main text, the steady state of the Kittel mode above the parametric instability threshold can be mapped on a degenerate two-level Ising pseudo-spin that is characterized by two opposite precession phases. The transition between these two states is reminiscent of the thermally activated or quantum tunneling of the magnetization in uniformly magnetized nanoparticle or molecular magnets [3–5]. In the absence of the

$\pm \vec{\mathcal{K}}$ modes, the physics of the pseudo-spin of the Kittel mode is similar to a bistable magnetization, where the phase space of the former is the infinite 2D plane of the Kittel mode harmonic oscillator quasi-position and quasi-momentum and the 2D Bloch sphere in the latter. The details of the free energy landscape on the phase spaces determine the competition between tunneling or thermally activated hopping frequencies, but there are some universal features as well. For example, with increasing the parametric excitation power and in the absence of $\pm \vec{\mathcal{K}}$ modes, the pseudo spin of the Kittel mode increases while the hopping frequency decreases [see Sec. II B], similar to the effect of increasing the size of a nanomagnet that leads to decreasing hopping rates. In this work, we control the Kittel mode pseudo-spin by the mixing with $\pm \vec{\mathcal{K}}$ modes [see Sec. IV and Fig. 4 in the main text].

A. Number states

We work with a finite basis set $N = N_0 N_{\vec{\mathcal{K}}_s}$, where $N_{0(\vec{\mathcal{K}}_s)}$ is the cutoff number of Fock states of the $0(\vec{\mathcal{K}}_s)$ mode. The Lindblad master Eq. (1) can then be written as $\partial_t \mathcal{Z} = \mathcal{L} \mathcal{Z}$, where the Liouvillian \mathcal{L} is a $N^2 \times N^2$ matrix and \mathcal{Z} is the density matrix ρ rearranged into a vector with N^2 elements. The steady state \mathcal{Z}_{ss} is the eigenvector of \mathcal{L} with eigenvalue $\mathcal{E}_{ss} = 0$. The time-dependent density matrix can be expanded as

$$\mathcal{Z}_{\text{phys}}(t) = \sum_i \mathcal{M}_i e^{\mathcal{E}_i t} \mathcal{Z}_i, \quad (14)$$

where the sum runs over the N^2 eigenstates, and $\mathcal{M}_i = \mathcal{Z}_i^T \mathcal{Z}_{\text{phys}}(0)$. $\forall i \neq ss \implies \text{Re} \mathcal{E}_i < 0$ and $\lim_{t \rightarrow \infty} \mathcal{Z}_{\text{phys}} = \mathcal{Z}_{ss}$.

We may model the magnon parametron by two coherent states of a harmonic oscillator separated by a high barrier in position-momentum phase space. An eigenvalue \mathcal{E}_{tnl} that satisfies $\text{Im} \mathcal{E}_{\text{tnl}} = 0$ is then associated to hopping. Since this rate is small compared to other fluctuations and so is $|\mathcal{E}_{\text{tnl}}|$ [6], we can calculate it accurately with a small basis set. We analyze the associated tunneling eigenvector \mathcal{Z}_{tnl} starting from an initial coherent state in one of the two Ising valleys $\mathcal{Z}_{\text{phys}}(t=0)$. To leading order in the interaction $\mathcal{Z}_{\text{phys}}(0) \approx \mathcal{Z}_{ss} + \mathcal{M}_{\text{tnl}} \mathcal{Z}_{\text{tnl}}$ and $\mathcal{Z}_{\text{phys}}(\infty) \approx \mathcal{Z}_{ss}$. It is convenient here to work with the non-negative Husimi function $Q(\alpha) = \langle \alpha | \rho_{\text{phys}} | \alpha \rangle / \pi > 0$, where $|\alpha\rangle$ is a coherent state and the $N^2 \times N^2$ density matrix ρ_{phys} contains all elements of the vector $\mathcal{Z}_{\text{phys}}$. Figure 3 of the main text shows that above the threshold and at long times the two valleys become symmetrically occupied with two identical maxima of $Q(\alpha)$ representing two mirror-symmetric coherent states. The latter corresponds to $Q(\alpha, \infty)$ for $\mathcal{Z}_{\text{phys}}(\infty) = \mathcal{Z}_{ss}$, whereas the initial $Q(\alpha, 0)$ corresponding to $\mathcal{Z}_{\text{phys}}(0)$ that we assumed is a coherent state at one of the valleys, has only one peak at that valley. The

decomposition $\mathcal{Z}_{\text{phys}}(0) = \mathcal{Z}_{ss} + \mathcal{M}_{\text{tnl}}\mathcal{Z}_{\text{tnl}}$ implies that the overlap of \mathcal{Z}_{tnl} with two coherent states at the two valleys should have opposite sign in order to cancel \mathcal{Z}_{ss} at one of the valleys and add to it at the other valley, for the $Q(\alpha, 0)$ to have only one peak at one of the valleys and the integration of $Q(\alpha, 0)$ over the phase space to remain equivalent to that of $Q(\alpha, \infty)$.

Let us first ignore $\vec{\mathcal{K}}_s$ and only consider the parametrically excited Kittel mode with self-Kerr nonlinearity. Figure S1(a) shows the absolute value of the overlap $|\mathcal{Z}_{ss}^T \mathcal{Z}_\alpha|$ between the steady state with the elements of the coherent state density matrix $|\alpha\rangle\langle\alpha|$ arranged into the vector \mathcal{Z}_α , where $\alpha = x_0 + ip_0$. $|\mathcal{Z}_{\text{tnl}}^T \mathcal{Z}_\alpha| = |\mathcal{Z}_{ss}^T \mathcal{Z}_\alpha|$, as expected. Fig. S1(b) shows that $\text{Re} \mathcal{Z}_{ss}^T \mathcal{Z}_\alpha$ is symmetric with respect to $(x_0 = 0, p_0 = 0)$, while Fig. S1(c) indicates that $\text{Re} \mathcal{Z}_{\text{tnl}}^T \mathcal{Z}_\alpha$ is antisymmetric (and the same holds for the imaginary parts).

When the Suhl instability of the Kittel mode parametron drives the $\vec{\mathcal{K}}_s$ mode, there are two tunneling eigenvalues $\mathcal{E}_{\text{tnl},1(2)}$. The Kittel mode hopping frequency is $\mathcal{F} = -\mathcal{E}_{\text{tnl},1}$ when $|\mathcal{Z}_{\text{tnl},1}^T \mathcal{Z}_\alpha| = |\mathcal{Z}_{ss}^T \mathcal{Z}_\alpha| \forall \alpha$, otherwise $\mathcal{F} = -\mathcal{E}_{\text{tnl},2}$.

B. Kittel mode parametric oscillator

Here, we address parametrically driven Kittel mode with finite self-Kerr non-linearity K_0 but without interactions with other magnons, equivalent to a Duffing oscillator. The Fokker-Planck equation for the Wigner distribution function to leading order in the derivatives with respect to coherent states α and α^* then reduces to

$$\begin{aligned} \dot{W}(\alpha, \alpha^*) &= \frac{\partial}{\partial \alpha} [\alpha + i\alpha^* (\mu + 2K_0\alpha^2)] + \\ &\quad \frac{1}{2} \frac{\partial^2}{\partial \alpha \partial \alpha^*} (1 + 2n_{\text{th}}) + \text{H.c.}, \end{aligned} \quad (15)$$

where $K_0 = 2\mathcal{Q}\mathcal{D}_{0,0,0,0}/\xi_0$ and $\mu = 2P_0/\xi_0$. With $\alpha = x_0 + ip_0$,

$$\dot{W}(x_0, p_0) = \left[-\frac{\partial}{\partial \mathcal{X}_i} \mathcal{A}_i + \frac{1}{2} \frac{\partial^2}{\partial \mathcal{X}_i \partial \mathcal{X}_j} D_{i,j} \right] W(x_0, p_0), \quad (16)$$

$\mathcal{X} = [x_0, p_0]$, $\mathcal{A}_1 = -[x_0 - 4K_0(x_0^2 + p_0^2) + 2\mu p_0]$, $\mathcal{A}_2 = -[p_0 + 4K_0(x_0^2 + p_0^2) + 2\mu x_0]$, and $D_{i,j} = \delta_{i,j}(1 + 2n_{\text{th}})/2$. The maxima of W are the steady-state mean-field amplitudes $\alpha_0 = |\alpha_0|e^{i\phi_0}$ that follow from the first term and its conjugate (drift) of Eq. (15),

$$\begin{aligned} i\mu\alpha_0^* + \alpha_0 + 2iK_0|\alpha_0|^2\alpha_0 &= 0, \\ -i\mu\alpha_0 + \alpha_0^* - 2iK_0|\alpha_0|^2\alpha_0^* &= 0. \end{aligned} \quad (17)$$

Hence, $|\alpha_0|^2 = \sqrt{\mu^2 - 1}|K_0|/2$, and $2\phi_0 = \arg[-K_0\sqrt{\mu^2 - 1}/\mu|K_0| + i/\mu]$.

In the steady state [1, 2]

$$A_i W = \frac{1}{2} \frac{\partial}{\partial \mathcal{X}_i} D_{i,j} W. \quad (18)$$

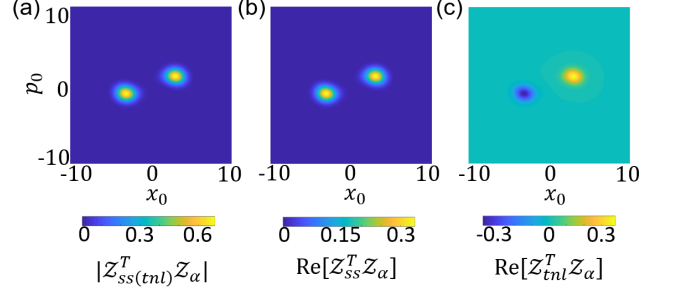


FIG. S1. (a) The modulus of the overlap of the Liouvillian eigenvectors $\mathcal{Z}_{ss(\text{tnl})}$ with the vector corresponding to the density matrix of the coherent state \mathcal{Z}_α , $\alpha = x_0 + ip_0$, i.e. $|\mathcal{Z}_{ss(\text{tnl})}^T \mathcal{Z}_\alpha|$ (b) $\text{Re}[\mathcal{Z}_{ss}^T \mathcal{Z}_\alpha]$. (c) $\text{Re}[\mathcal{Z}_{\text{tnl}}^T \mathcal{Z}_\alpha]$.

Assuming a solution of the form $W(x_0, p_0) = \mathcal{N}e^{-\Phi(x_0, p_0)}$, where \mathcal{N} is the normalizing constant

$$-\frac{\partial \Phi}{\partial \mathcal{X}_i} = 2D_{i,j}^{-1} \left[A_j - \frac{1}{2} \frac{\partial D_{j,l}}{\partial \mathcal{X}_l} \right]. \quad (19)$$

When Φ is a proper potential with $\partial^2 \Phi / \partial x_0 \partial p_0 = \partial^2 \Phi / \partial p_0 \partial x_0$, which ensures that the solutions of Equations (19) do not depend on the path of integration, i.e.

$$\Phi = - \int_0^x \frac{\partial \Phi}{\partial \mathcal{X}_i} d\mathcal{X}_i.$$

Strictly speaking $\partial^2 \Phi / \partial x_0 \partial p_0 = 4[-4K_0(3p_0^2 + x_0^2) + 2\mu]/(1 + 2n_{\text{th}})$ and $\partial^2 \Phi / \partial p_0 \partial x_0 = 4[4K_0(3x_0^2 + p_0^2) + 2\mu]/(1 + 2n_{\text{th}})$ are not equal. However, in the region between the two minima $(x_{0,m}, p_{0,m})$, $|4K_0|(3x_{0,m}^2 + p_{0,m}^2) \ll 2\mu$ and $|4K_0|(x_{0,m}^2 + 3p_{0,m}^2) \ll 2\mu$. For very small $\mu > 1$ above the threshold $\phi_{0,m} \approx \pi/4$, and $(x_{0,m}, p_{0,m}) = (0, \pm|\alpha_0|)$. Therefore, $12|K_0\alpha_0|^2 = 6\sqrt{\mu^2 - 1} \ll 2\mu$, i.e., $1 < \mu \ll \sqrt{9/8}$, approximately satisfies the potential conditions. The transition time in this potential barrier approximation [6, 7],

$$\tau = \frac{2\pi}{\xi_0} \left[\frac{\Phi_{x_0 x_0}(0, 0)}{\Phi_{x_0 x_0}(0, |\alpha_0|)\Phi_{p_0 p_0}(0, |\alpha_0|)\Phi_{p_0 p_0}(0, 0)} \right]^{1/2} \times \exp[\Phi(0, |\alpha_0|) - \Phi(0, 0)], \quad (20)$$

where $\Phi_{\mathcal{X}_i \mathcal{X}_i} = \partial^2 \Phi / \partial \mathcal{X}_i^2$. Hence

$$\tau = \frac{\pi(1 + 2n_{\text{th}})}{2\xi_0} \exp \left[\frac{\sqrt{\mu^2 - 1}}{(1 + 2n_{\text{th}})|K_0|} \right]. \quad (21)$$

Kinsler and Drummond [6] studied the transition frequency of a parametron in the presence of nonlinear damping rather than self-Kerr nonlinearity, at zero temperature. Because of the similarity of the steady states governed by either the self-Kerr interaction or the nonlinear damping (see below), and the validity of the analytic

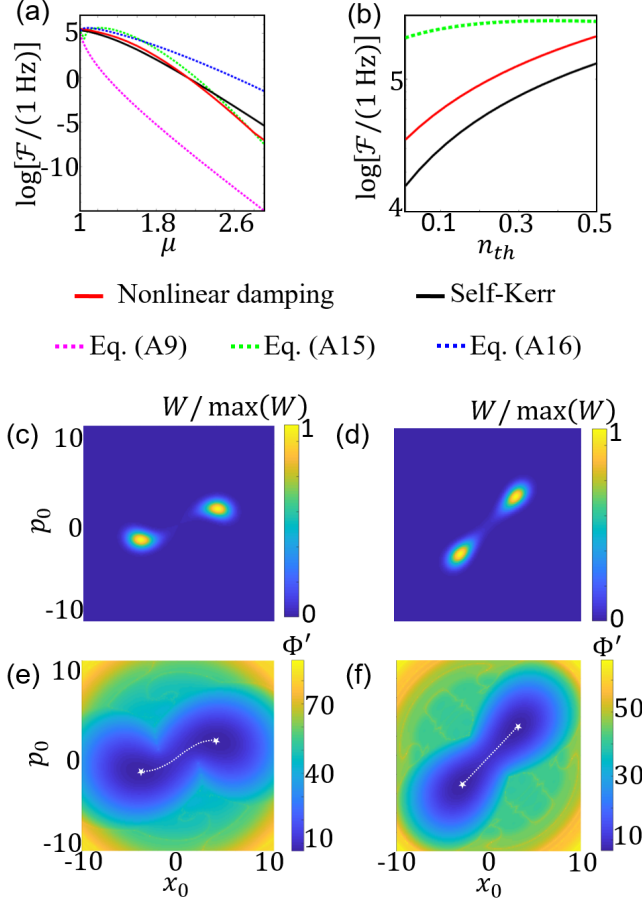


FIG. S2. (a) The dependence of the tunneling frequency \mathcal{F} on μ from quantum calculations for nonlinear damping and self-Kerr nonlinearity. \mathcal{F} from analytical equations Eq. (21), Eq. (27), and Eq. (28) also shown. $n_{th} = 0$. (b) The dependence of \mathcal{F} on n_{th} for $\mu = 1.4$. In (a)-(b), $\mathcal{Q} = 5 \times 10^8$. (c) and (d) The Wigner function for self Kerr nonlinearity and nonlinear damping, respectively, while $\mu = 1.4$. (e) and (f) The quasi-potential, $\Phi' = -\ln W$, corresponding to (c) and (d). The stars are the minima of Φ' and the dashed lines are along the minimal gradient path. In (c)-(f), $\mathcal{Q} = 5 \times 10^8$. In (a)-(f), $H_{ext} = 40$ mT.

treatment for a large μ interval in the latter case, we extend the analysis in [6] to nonzero temperatures through the Lindblad operator,

$$L_{NL} = \xi_{NL} (n_{th} + 1) \left(2c_0^\dagger \rho c_0^{\dagger 2} - c_0^{\dagger 2} c_0^2 \rho - \rho c_0^{\dagger 2} c_0^2 \right) + \xi_{NL} n_{th} \left(2c_0^{\dagger 2} \rho c_0^2 - c_0^2 c_0^{\dagger 2} \rho - \rho c_0^2 c_0^{\dagger 2} \right), \quad (22)$$

where ξ_{NL} is the nonlinear dissipation parameter. Nonlinear dissipation should exist under parametric excitation conditions due to photon dissipation and four-magnon scattering to thermal magnons, but in contrast to the self-Kerr term, its value for YIG is unknown. For simplicity, we set $K_0 = 0$ and assume an imaginary parametric excitation $iP_0 c_0^\dagger c_0^\dagger + H.c.$, where P_0 and thereby

$\mu = 2P_0/\xi_0$ are real, i.e. a phase shift of the drive by $\pi/2$ relative to the global phase reference. The Wigner function then solves

$$\frac{dW}{dt} = \left\{ \frac{\partial}{\partial \alpha} [\alpha - \alpha^* (\mu - g_{NL} \alpha^2)] + \frac{(1 + 2n_{th})}{2} \frac{\partial^2}{\partial \alpha \partial \alpha^*} (1 + g_{NL} \alpha \alpha^*) + H.c. \right\} W, \quad (23)$$

where $g_{NL} = 4\xi_{NL}/\xi_0$. In terms of (x_0, p_0) , where $\alpha = x_0 + ip_0$, Eq. (23) can be written in the form of Eq. (16), where $A_1 = -x_0 (1 + g_{NL} x_0^2 - \mu)$, $A_2 = -p_0 (1 + g_{NL} p_0^2 + \mu)$, $D_{11} = (1 + 2n_{th}) (1 + 2g_{NL} x_0^2) / 4$, and $D_{22} = (1 + 2n_{th}) (1 + 2g_{NL} p_0^2) / 4$. The resulting 2D FPE does not have a potential solution, because $\partial^2 \Phi / \partial x_0 \partial p_0 \neq \partial^2 \Phi / \partial p_0 \partial x_0$ [see Eq. (19)]. However, the states always relax towards $p_0 = 0$ because A_2 has the opposite sign to p_0 . The FPE for $p_0 = 0$ is only a function of x_0 [6],

$$\frac{dW_{1D}}{dt} = \left\{ \frac{\partial}{\partial x_0} [x_0 (1 + g_{NL} x_0^2 - \mu)] + \frac{1}{4} \frac{\partial^2}{\partial x_0^2} [(1 + 2n_{th}) (1 + 2g_{NL} x_0^2)] \right\}. \quad (24)$$

All 1D FPE equations have potential solutions [2], and Eqs. (19) and (24) lead to

$$\Phi(x_0) = \frac{1}{(1 + 2n_{th})} \left[x_0^2 - \frac{2R + 1}{2g_{NL}} \ln (2g_{NL} x_0^2 + 1) \right], \quad (25)$$

where $R = \mu - g_{NL} (1 + 2n_{th}) - 1$. The extrema of Φ_{x_0} are at $x_{0,s} = 0$ (saddle point) and $x_{0,m} = \pm \sqrt{R/g_{NL}}$ (the two minima). The transition time between the two minima is

$$\tau = \frac{2\pi}{\xi_0} \left[\frac{1}{\Phi_{x_0 x_0}(x_{0,m}) \Phi_{x_0 x_0}(x_{0,s})} \right]^{1/2} \times \exp [\Phi(x_{0,s}) - \Phi(x_{0,m})], \quad (26)$$

which with Eq. (25) leads to

$$\tau = \frac{\pi}{2\xi_0} \left[\frac{(1 + 2n_{th})^2 (1 + 2R)}{2R^2} \right]^{1/2} \times \exp \left\{ \frac{1}{2g_{NL} (1 + 2n_{th})} [(2R + 1) \ln (2R + 1) - 2R] \right\}. \quad (27)$$

In Fig. S2(a), we compare the hopping frequency \mathcal{F} from a numerical solution of the master equation corresponding to either g_{NL} or K_0 being finite, with the analytical Eqs. (21) and (27), respectively, for $n_{th} = 0$ and a scaling coefficient $\mathcal{Q} = 5 \times 10^8$ of the four-magnon scattering coefficients $\mathcal{D} \rightarrow \mathcal{Q}\mathcal{D}$ that reduces the Hilbert space to a manageable size. We illustrate the results by choosing $g_{NL} = |K_0|$. Figure S2(a) shows that Eq. (27) approximately agrees with numerical calculation [6],

whereas Eq. (21) is too small for $\mu > 1$, i.e. above the parametric pumping threshold. because the assumption of small μ is not valid anymore. We may improve Eq. (27) by adopting a distance between the two minima for the nonlinear damping that equals that of the self-Kerr nonlinearity, i.e., $(\mu' - 1)/g_{NL} = \sqrt{\mu^2 - 1}/2|K_0|$,

$$\tau = \frac{\pi}{2\xi_0} \left[\frac{(1 + 2n_{th})^2 (1 + 2R')}{2R'^2} \right]^{1/2} \times \exp \left[\frac{1}{2g_{NL} (1 + 2n_{th})} \{ (2R' + 1) \ln (2R' + 1) - 2R' \} \right]. \quad (28)$$

where $R' = \sqrt{\mu^2 - 1}/2 + 1 - g_{NL}(1 + 2n_{th}) - 1$. The blue dashed line in Fig. S2(a) shows that the transition frequency from Eq. (28) now overestimates \mathcal{F} for the self-Kerr nonlinearity, and can be used as an analytical upper bound when $n_{th} = 0$.

Figure S2(b) shows the dependence of \mathcal{F} on n_{th} for $\mu = 1.4$ and $\mathcal{Q} = 5 \times 10^8$ for both cases of self-Kerr and nonlinear damping. Figure S2(b) shows that with increasing temperature, \mathcal{F} increases as expected. \mathcal{F} according to Eq. (27) monotonically increases with temperature up to $n_{th} \approx 0.5$ and is larger than the numerical calculations [see the green dashed line in Fig. S2(b)]. Figure S2(b) is for $\mathcal{Q} = 5 \times 10^8$, which means that the potential is 5×10^8 times shallower than the physical ($\mathcal{Q} = 1$) case [see Eq. (25)]. Therefore, we can estimate that $n_{th} = 0.5$ when $\mathcal{Q} = 5 \times 10^8$ corresponds to $0.5 \times 5 \times 10^8 \sim 2.5 \times 10^8$, i.e. $T \approx 10^7$ K when $\mathcal{Q} = 1$. We confirm that for any μ , when $\mathcal{Q} = 5 \times 10^8$, and $n_{th} < 0.5$, \mathcal{F} from Eq. (28) is larger than the numerical calculation for the case of self-Kerr nonlinearity. Therefore, for the physical case, Eq. (28) provides a reliable upper bound of \mathcal{F} for $T < 10^7$ K and every value of μ .

Figures S2(e) and (f) show the (quasi-)potential $\Phi' = -\ln W$, corresponding to Figs. S2(c) and (d), respectively. The white stars indicate the minima of Φ' , and the white dashed line connects the two minima through the minimal gradient path that govern the transition. The latter line is not straight for the self-Kerr nonlinearity in contrast to that for nonlinear damping, supporting the validity of the 1D assumption leading to Eq. (24). Apart from the twist in the quasi-potential of Fig. S2(e), it is approximately the same as that of Fig. S2(f), leading to the similar scale of \mathcal{F} for self-Kerr nonlinearity and nonlinear damping. In conclusion, while a hypothetical substantial non-linear damping should affect the numbers but not the phenomenology and can be captured by re-scaling the Kerr constant.

III. GAUSSIAN BIPARTITE ENTANGLEMENT

Here, we analyze the bipartite Gaussian entanglement of the Kittel mode fluctuations with the $\vec{\mathcal{K}}_s$ standing

wave in a magnonic dot. “Gaussian” refers to the assumption that the fluctuations in the steady states can be enveloped by a finite ellipse and the second moments describe auto and cross correlations well. “Bipartite entanglement” means that the fluctuations cannot be reproduced by a product state of Kittel mode and $\vec{\mathcal{K}}_s$ fluctuations. It is caused by interactions that we capture by the mean-field Hamiltonian with two terms called “beam splitter” and “two-mode squeezing”

$$H_{MF} = \eta \delta c_0^\dagger \delta c_{\vec{\mathcal{K}}_s} + \mathbf{g} \delta c_0 \delta c_{\vec{\mathcal{K}}_s} + \text{H.c.}, \quad (29)$$

where $\eta = K_1 \alpha_0 \alpha_{\vec{\mathcal{K}}_s}^* + K_2 \alpha_0^* \alpha_{\vec{\mathcal{K}}_s}$ and $\mathbf{g} = K_1 \alpha_0^* \alpha_{\vec{\mathcal{K}}_s}^*$.

It is convenient to rewrite the Fokker-Planck equation of the Wigner function Eq. (16) as

$$\dot{W}(\vec{\mathcal{X}}) = \left[-\frac{\partial}{\partial \mathcal{X}_i} \mathcal{A}_{i,j} \mathcal{X}_j + \frac{1}{2} \frac{\partial^2}{\partial \mathcal{X}_i \partial \mathcal{X}_j} D_{i,j} \right] W(\vec{\mathcal{X}}), \quad (30)$$

where $\vec{\mathcal{X}} = [\delta x_0, \delta p_0, \delta x_{\vec{\mathcal{K}}_s}, \delta p_{\vec{\mathcal{K}}_s}]$, and $[\mathcal{A}]_{4 \times 4}$ is a mean-field drift matrix. The diffusion matrix $D = \xi (2n_{th} + 1) / 2 [I]_{4 \times 4}$, where I is the unit matrix while

$$\mathcal{A} = \begin{bmatrix} \xi/2 & 0 & -\mathbf{b} & \mathbf{a} \\ 0 & \xi/2 & \mathbf{c} & \mathbf{d} \\ -\mathbf{d} & \mathbf{a} & \xi/2 & 0 \\ \mathbf{c} & \mathbf{b} & 0 & \xi/2 \end{bmatrix}, \quad (31)$$

where $\mathbf{a} = \text{Re}(\mathbf{g} - \eta)$, $\mathbf{b} = \text{Im}(\mathbf{g} + \eta)$, $\mathbf{c} = \text{Re}(\mathbf{g} + \eta)$, and $\mathbf{d} = \text{Im}(\mathbf{g} - \eta)$. The steady state covariance matrix with elements $\langle \mathcal{X}_i \mathcal{X}_j \rangle$,

$$\mathcal{V}_{ss} = \begin{bmatrix} \Upsilon & \Xi \\ \Xi^T & \Upsilon' \end{bmatrix} \quad (32)$$

solves

$$\mathcal{A} \mathcal{V}_{ss} + \mathcal{V}_{ss} \mathcal{A} = -D. \quad (33)$$

The distillable bipartite entanglement is bounded from above by the logarithmic negativity [8–10],

$$E_{LN} = \max[0, -\ln(\zeta)] \quad (34)$$

$$\zeta^2 = \left[f(\mathcal{V}_{ss}) - \sqrt{f^2(\mathcal{V}_{ss}) - 4|\mathcal{V}_{ss}|} \right], \quad (35)$$

where $f(\mathcal{V}_{ss}) = \det \Upsilon + \det \Upsilon' - 2 \det \Xi$ and \det indicates the determinant of a matrix.

Assuming without loss of generality $\text{Im} \mathbf{g} = \text{Im} \eta = 0$, the solution of Eq. (33) are

$$\begin{aligned} \mathcal{V}_{ss,1,1} &= \frac{2n(2\mathbf{a}\mathbf{c} - \xi^2/4 - 2\mathbf{a}^2)}{\xi(4\mathbf{a}\mathbf{c} - \xi^2/4)}, \\ \mathcal{V}_{ss,1(4),4(1)} &= \frac{n(\mathbf{a} + \mathbf{c})}{(4\mathbf{a}\mathbf{c} - \xi^2/4)}, \\ \mathcal{V}_{ss,2,2} &= \frac{2n(2\mathbf{a}\mathbf{c} - \xi^2/4 - 2\mathbf{c}^2)}{\xi(4\mathbf{a}\mathbf{c} - \xi^2/4)}, \\ \mathcal{V}_{ss,2(3),3(2)} &= \mathcal{V}_{ss,1(4),4(1)}, \end{aligned} \quad (36)$$

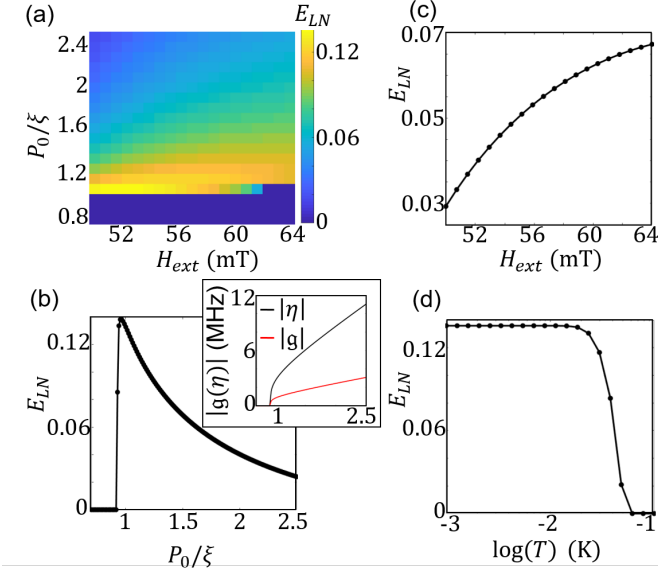


FIG. S3. Results from an analytical model for Gaussian magnon entanglement. (a) The logarithmic negativity E_{LN} as a function of H_{ext} and P_0/ξ . Panels (b)-(d) are line cuts out of (a). (b) Dependence of E_{LN} and $|g(\eta)|$ (inset) on P_0/ξ at $H_{ext} = 52$ mT. (c) E_{LN} dependence on H_{ext} at $P_0/\xi = 2$. (d) E_{LN} dependence on T at $H_{ext} = 50$ mT and $P_0/\xi = 1$.

and lead to

$$\zeta^2 = \frac{n^2 \xi^2}{4\Omega} \left[\mathcal{J} + \xi^2 (\mathbf{a} + \mathbf{c}) / 4 - \xi (\mathbf{a} + \mathbf{c}) \sqrt{\mathcal{J}} \right], \quad (37)$$

where $n = \xi(2n_{th} + 1)/2$, $\mathcal{J} = (2\mathbf{a}\mathbf{c} - \xi^2/4 - 2\mathbf{a}^2) / (2\mathbf{a}\mathbf{c} - \xi^2/4 - 2\mathbf{c}^2)$, and $\Omega = \xi^4 (4\mathbf{a}\mathbf{c} - \xi^2/4)^2 / 16$.

We proceed by the rather rough approximation that beyond the Suhl instability the Kittel mode mean-field $\alpha_0 = |\alpha_0|e^{i\phi_0}$ is constant with

$$|\alpha_0|^2 = \frac{1}{2|\mathcal{D}_{0,0,0,0}|} \sqrt{P_0^2 - \left(\frac{\xi}{2}\right)^2},$$

$$\phi_0 = -\arg \left[\frac{-i}{P_0} \left(\frac{\xi}{2} + 2i\mathcal{D}_{0,0,0,0}|\alpha_0|^2 \right) \right] / 2, \quad (38)$$

which is the steady state of the self Hamiltonian $(P_0 c_0^\dagger c_0^\dagger + \text{H.c.}) + \mathcal{D}_{0,0,0,0} c_0^\dagger c_0^\dagger c_0$. The mean field $\alpha_{\vec{k}_s}$ is then the steady state of the effective Hamiltonian $\Delta' \omega_{\vec{k}_s} c_{\vec{k}_s}^\dagger c_{\vec{k}_s} + (K_2 \alpha_0^2 c_{\vec{k}_s}^\dagger c_{\vec{k}_s}^\dagger + \text{H.c.}) + K_5 c_{\vec{k}_s}^\dagger c_{\vec{k}_s} c_{\vec{k}_s}^\dagger c_{\vec{k}_s}$, where $\Delta' \omega_{\vec{k}_s} = \Delta \omega_{\vec{k}_s} + K_1 |\alpha_0|^2$. $K_1 = \mathcal{D}_{0,0,\pm\vec{k},\pm\vec{k}}$, $K_2 = \mathcal{D}_{0,\vec{k},0,-\vec{k}}$, $K_5 = 2K_3 + K_4$, $K_3 = \mathcal{D}_{\pm\vec{k},\pm\vec{k},\pm\vec{k},\pm\vec{k}}$, and $K_4 = \mathcal{D}_{\pm\vec{k},\pm\vec{k},\mp\vec{k},\mp\vec{k}}$ [cf. Eq. (4) in the main text to deter-

mine],

$$\alpha_{\vec{k}_s} = |\alpha_{\vec{k}_s}| e^{i\phi_{\vec{k}_s}},$$

$$|\alpha_{\vec{k}_s}|^2 = \frac{1}{2|K_5|} \sqrt{K_2^2 |\alpha_0|^4 - \left(\frac{\xi}{2}\right)^2 - \Delta' \omega_{\vec{k}_s}},$$

$$\phi_{\vec{k}_s} = \arg \left[\frac{-i}{2\alpha_0^2} \left(-\frac{\xi}{2} - 2iK_5 |\alpha_{\vec{k}_s}|^2 - i\Delta' \omega_{\vec{k}_s} \right) \right] / 2. \quad (39)$$

Figure S3(a) shows the resulting E_{LN} as a function of P_0/ξ and H_{ext} . At a fixed H_{ext} , E_{LN} jumps to a nonzero value just above the Suhl instability threshold to subsequently decrease with increasing P_0/ξ [see also Fig. S3(b)]. For $P_0/\xi > 1.4$, E_{LN} increases with H_{ext} [see also Fig. S3(c)]. Figure S3(d) shows that E_{LN} decreases with T and drops to ~ 0.01 at around $T \sim 100$ mK. The good agreement with the numerical results in Fig. 5 of the main text confirm the validity of the model assumptions.

The self-consistent mean-fields $|g|$ and $|\eta|$ monotonically increase with P_0 , and eventually $|\eta| \gg |g|$ [see the inset of Fig. S3(b)]. For large P_0 , $\mathcal{J} \approx \Omega \approx (4\eta^2 + \xi^2/4)^2$ [defined after Eq. (37)] and

$$\zeta^2 = (2n_{th} + 1) \left[1 + \frac{\mathbf{g}^2 \xi^2 / 4 - \xi \mathbf{g} (4\eta^2 + \xi^2 / 4)}{(4\eta^2 + \xi^2 / 4)^2} \right], \quad (40)$$

leading to $\lim_{\eta \rightarrow \infty} \zeta^2 = 1$ and $\lim_{P_0 \rightarrow \infty} E_{LN} = 0$. The entanglement vanishes for large P_0 [see S3(b)], as it does in the numerical calculations [see Fig. 5(a) of the main text].

Just above the Suhl instability threshold, $\xi/2 \gg \mathbf{g}, \eta$, i.e., $\mathcal{J} \approx \Omega \approx \xi^4/16$, and

$$\zeta^2 = (2n_{th} + 1) \frac{\xi^4 + 4\mathbf{g}^2 \xi^2 - 4\mathbf{g} \xi^3}{\xi^4}. \quad (41)$$

while below it, $\mathbf{g} = 0$, and Eq. (37) leads to $\zeta^2 = 1$, i.e., $E_{LN} = 0$. Above the Suhl instability, \mathbf{g} increases with P_0 , and according to Eq. (41), just above the threshold, ζ^2 drops below 1 and decreases, i.e., according to Eq. (34) E_{LN} becomes nonzero and increases [see Figs. S3(b) and 5(a) of the main text].

According to Eq. (40), ζ^2 increases with n_{th} , i.e., E_{LN} decreases as $-\ln[(2n_{th} + 1)] + E_{LN}(T = 0)$ [see Fig. S3(d)]. A magnetic field freezes n_{th} out and $E_{LN}(T) \rightarrow E_{LN}(T = 0)$.

In spite of the approximations, the analytical model appears to explain the qualitative physics well, but we emphasize that they cannot replace the accurate numerical calculations presented in Figs. 5(a)-(c) of the main text.

IV. SUHL INSTABILITY AND BIFURCATION OF THE LIMIT CYCLES

In Sec. IIB, we discussed the hopping frequency \mathcal{F} of the Kittel mode parametron in the absence of interac-

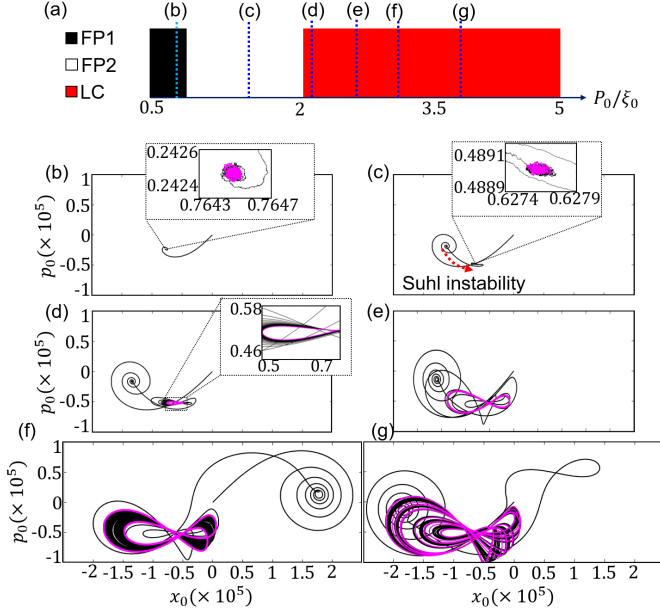


FIG. S4. (a) The dynamical steady states of the magnetic dot calculated as a function of P_0/ξ_0 , for $H_{ext} = 40$ mT. The blue dashed lines indicate P_0/ξ_0 that corresponding to the time traces plotted in panels (b)-(g). (b) $P_0/\xi_0 = 0.86$, FP1. (c) $P_0/\xi_0 = 1.51$, FP2. The red dashed arrow indicates the Suhl instability due to parametric pumping. (d) $P_0/\xi_0 = 2.06$, LC. (e) $P_0/\xi_0 = 2.34$, LC. (f) $P_0/\xi_0 = 2.89$, LC. (g) $P_0/\xi_0 = 3.81$, LC. In (b)-(g), the black trajectories are from $t = 0$ to $t = 40 \mu s$, and the purple trajectories are from $t = 30 \mu s$ to $t = 40 \mu s$. The insets in (b)-(d) are zooms of the main panels.

tions with $\pm \vec{k}$ pair. We showed in the main text that for P_0 above the Suhl instability that leads to the decay into finite momentum magnon pairs the transition rate increases substantially when the steady state is a limit cycle (LC). Here, we discuss the LC trajectories as a function of P_0 up to just below the jump in \mathcal{F} . Figure S4(a) presents our results for the steady states as a function of P_0/ξ_0 (see also Fig. 2 of the main text), for $H_{ext} = 40$ mT, and indicates the respective value of P_0/ξ_0 corresponding to Figs. S4(b)-(g) in increasing order. In Figs. S4(b)-(g), we assumed $T = 0$ and an initial random (x_0, p_0) near the origin. The black trajectories are from $t = 0$ to $t = 40 \mu s$, whereas the purple ones are the steady state trajectories from $t = 30 \mu s$ to $t = 40 \mu s$. Figure S4(b) is the fixed point FP1 steady state below the Suhl instability. Figure S4(c) is the FP2 fixed point steady state generated by the Suhl instability. The Ising spin states of FP1 and FP2 are extremely stable, with astronomically small hopping frequencies.

Figure S4(d) correspond to a microwave power just above the bifurcation to a LC steady state. Initially, the LC has a small amplitude that increases with P_0/ξ_0 to develop a pronounced butterfly shape [see Fig. S4(e)]. For even larger P_0/ξ_0 , the limit cycle bifurcates. In the steady state in Fig. S4(f) we observe 2 LC butterflies and

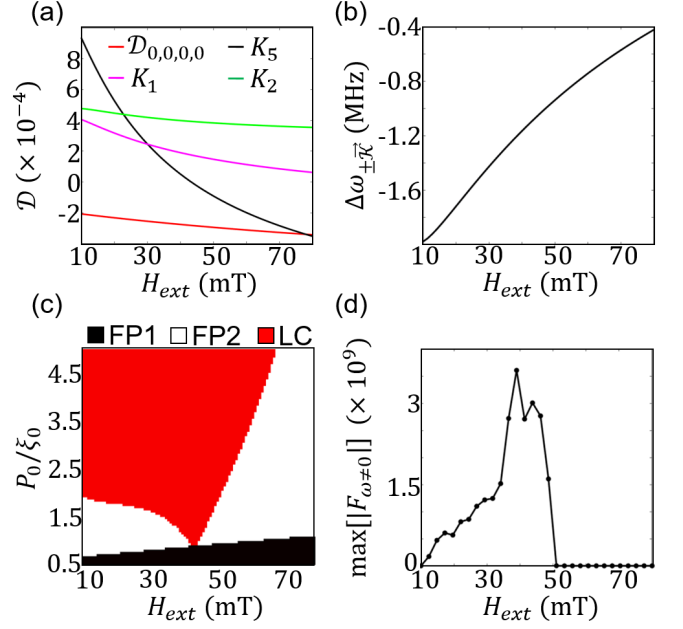


FIG. S5. (a) The dependence of four-magnon scattering coefficients relevant to the dynamics on H_{ext} . (b) The dependence of $\Delta\omega_{\pm\vec{k}}$ on H_{ext} . (c) An analytical phase diagram [see Fig. 2(a) of the main text]. (d) The H_{ext} dependence of the peak of Fourier transform of $x_0(t)$, F_{ω} , at any $\omega \neq 0$, for $P_0/\xi_0 = 3.5$ [see Figs. 2(a) and 4(c) of the main text].

4 in Fig. S4(g). The increase in the LC radius and its multiplying indicates a shallower potential trench that confines the dynamics and a much broader probability distribution that is definitely not Gaussian. A shallower potential well or trench implies an increase in the hopping over the saddle point between the two Ising spin states.

Next, we discuss field dependence of the steady state phase diagram of Fig. 2(a) of the main text and the associate Ising spin flip rates. At a fixed P_0 , the steady states are governed by the four magnon scattering coefficients \mathcal{D} , and $\Delta\omega_{\pm\vec{k}}$, that in turn depend on H_{ext} . Figure S5(a) shows the dependence of $\mathcal{D}_{0,0,0,0}$, $K_1 = \mathcal{D}_{0,0,\pm\vec{k},\pm\vec{k}}$, $K_2 = \mathcal{D}_{0,\vec{k},0,-\vec{k}}$, and $K_5 = 2K_3 + K_4$ on H_{ext} , where $K_3 = \mathcal{D}_{\pm\vec{k},\pm\vec{k},\pm\vec{k},\pm\vec{k}}$ and $K_4 = \mathcal{D}_{\pm\vec{k},\pm\vec{k},\mp\vec{k},\mp\vec{k}}$. Figure S5(b) shows the dependence of $\Delta\omega_{\pm\vec{k}}$ on H_{ext} . As we discussed in the main text, the boundary of FP1 and FP2 [the green line in Fig. 2(a) of the main text] is the Suhl instability threshold. According to Eq. (4) of the main text

$$|\alpha_{0,\text{Suhl}}|^2 = \frac{1}{K_2^2 - K_1^2} \times \left(\Delta\omega_{\pm\vec{k}} K_1 + \sqrt{\Delta\omega_{\pm\vec{k}}^2 K_1^2 + (K_2^2 - K_1^2) \times (\xi_0^2/4 + \Delta\omega_{\pm\vec{k}}^2)} \right). \quad (42)$$

For $\xi_0 = 5$ MHz, $|\alpha_{0,\text{Suhl}}|^2 \approx \xi_0/2\sqrt{K_2^2 - K_1^2}$ decreases by a factor of $\sim 1/1.3$ when increasing H_{ext} from 10 mT

to 80 mT while $|\alpha_0|^2 \propto 1/|\mathcal{D}_{0,0,0,0}|$ decreases by a factor of $\sim 1/1.7$. The P_0 needed to drive the Suhl instability therefore increases slightly by a factor of $\sim 1.7/1.3$ in the field interval, as does the green line in Fig. 2(a) of the main text.

We can estimate the boundary between FP2 and LC phases by the same approximation that led to α_0 and $\alpha_{\vec{\kappa}_s}$ in Eqs. (39) and (40) above the threshold. The transition for a limit cycle by the mean field term $K_1\alpha_0^*\alpha_{\vec{\kappa}_s}^*\delta c_0\delta c_{\vec{\kappa}_s} + \text{H.c.}$ requires that

$$\left| K_1\alpha_{0,LC}\alpha_{\vec{\kappa}_s,LC} \right| = \xi_0/2, \quad (43)$$

where $\alpha_{0,LC}$ and $\alpha_{\vec{\kappa}_s,LC}$ are the mean fields at the FP2 to LC transition. For the same magnetic field interval and fixed P_0 , $|\alpha_0|^2 \propto 1/|\mathcal{D}_{0,0,0,0}|$ decreases by a factor of $\sim 1/1.7$. In $|\alpha_{\vec{\kappa}_s}|^2 \propto (K_2 + K_1)|\alpha_0|^2/|K_5| \propto (K_2 + K_1)/|K_5||\mathcal{D}_{0,0,0,0}|$, $(K_2 + K_1)/|\mathcal{D}_{0,0,0,0}|$ decreases by a factor of ~ 0.3 while $|K_5|$ decreases to zero at around 40 mT, and then increases to ~ 0.5 times of the initial

value, at 80 mT. K_1 monotonically decreases by a factor of $\sim 1/8$ with increasing H_{ext} in the same range. Therefore, P_0 corresponding to $|K_1\alpha_{0,LC}\alpha_{\vec{\kappa}_s,LC}|$ has a minimum at $H_{\text{ext}} \sim 40$ mT, and is larger by a factor of ~ 8 for $H_{\text{ext}} = 80$ mT than $H_{\text{ext}} = 10$ mT. Fig. S5(c) shows the boundaries between FP2, FP1 and LC as calculated from Eqs. (43) and (39)-(40) and captures the main features of the numerically exact phase diagram of Fig. 2(a) of the main text. The differences such as the strong drop of the FP2|LC boundary at intermediate fields are a consequence of the rough mean-field approximation.

We expect that for fixed P_0 beyond the LC transition the limit cycle oscillation amplitudes would be enhanced at $H_{\text{ext}} \sim 40$ mT. This is indeed consistent with the Ising spin hopping rate \mathcal{F} in Figs. 4(c) and (d) of the main text. F_ω , the Fourier transform of $x_0(t)$ may help to elucidate the correlation between the LC oscillation amplitude and \mathcal{F} since a peaked F_ω indicates that the steady state is a limit cycle. Figure S5(d) shows the dependence of this peak amplitude, $\max(|F_{\omega \neq 0}|)$ on H_{ext} that confirms the expectations.

-
- [1] H. J. Carmichael, *Statistical Methods in Quantum Optics*, Springer (1999).
 - [2] D. F. Walls and G. J. Milburn, *Quantum Optics*, Springer (2008).
 - [3] W. F. Brown, *Thermal Fluctuations of a Single-Domain Particle*, Phys. Rev. **130**, 1677 (1963).
 - [4] A. A. Kovalev, L. X. Hayden, G. E. W. Bauer, and Y. Tserkovnyak, *Macrospin Tunneling and Magnetopolaritons with Nanomechanical Interference*, Phys. Rev. Lett. **106**, 147203 (2011).
 - [5] K. Hayakawa, S. Kanai, T. Funatsu, J. Igarashi, B. Jinai, W. A. Borders, H. Ohno, and S. Fukami, “Nanosecond Random Telegraph Noise in In-Plane Magnetic Tunnel Junctions”, Phys. Rev. Lett. **126**, 11702 (2021).
 - [6] P. Kinsler and P. D. Drummond, *Quantum dynamics of the parametric oscillator*, Phys. Rev. A **43**, 6194 (1991).
 - [7] R. Landauer and J. A. Swanson, *Frequency Factors in the Thermally Activated Process*, Phys. Rev. **121**, 1668 (1961).
 - [8] G. Vidal and R. F. Werner, *Computable Measure of Entanglement*, Phys. Rev. A **65**, 032314 (2002).
 - [9] S. L. Braunstein and P. van Loock, *Quantum Information with Continuous Variables*, Rev. Mod. Phys. **77**, 513 (2005).
 - [10] G. Adesso and F. Illuminati, *Gaussian Measures of Entanglement versus Negativities: Ordering of Two-Mode Gaussian States*, Phys. Rev. A **72**, 032334 (2005).